

ABSTRACT

Title of Thesis: COMBINATORIAL EXPLORATION OF ARTIFICIAL
MULTIFERROIC THIN FILMS

Chuan-Lan Lin, Master of Science, 2004

Thesis directed by: Professor I. Takeuchi

Department of Materials Science and Engineering

Combinatorial synthesis consists of high throughput fabrication and rapid characterization of compositionally varying samples to speed up the process of materials development. In this thesis, synthesis of composition spreads of artificial multiferroic thin film heterostructures consisting of alternating layers of PbTiO_3 (PTO) - CoFe_2O_4 (CFO) has been demonstrated using our combinatorial pulsed laser deposition (PLD) system. In the spread samples, the average composition changes continuously from pure PTO to pure CFO so that we can observe the changes in physical properties as a function of average composition.

The coexistence of ferromagnetic and ferroelectric properties has been

observed in a large extended region between pure CFO and PTO. An unexpected peak in the dielectric property has been observed in the middle of the spread, and it was identified as the composition where the ferroelectric phase transition takes place in PTO doped with CFO. The T_c of ferroelectricity is found to be tunable from 500 °C to room temperature by controlling the average volume ratio of CFO and PTO. We have also found that the magnetic anisotropy in the materials changes by introducing PTO to CFO.

COMBINATORIAL EXPLORATION OF ARTIFICIAL MULTIFERROIC THIN FILMS

By
Chuan-Lan Lin

Thesis submitted to the Faculty of the Graduate School of the
University of Maryland, College Park in partial fulfillment
of the requirement for the degree of
Master of Science
2004

Advisory Committee:

Professor I. Takeuchi, Chairman/Advisor

Professor I. Lloyd

Professor L. Martinez-Miranda

© Copyright by
Chuan-Lan Lin
2004

Acknowledgements

I would like to take a chance to thank all the people who helped me on this thesis. First I would like to thank my advisor, Professor I. Takeuchi, for his advice during these two years, and my committee members, Professor I. Lloyd and Professor L. Martinez for giving valuable comments on my thesis.

I would also like to thank all the people in my research group. This thesis focused on fabrication of heterostructural thin films. I made all the samples using our pulsed laser deposition (PLD) system and performed measurements on them in collaboration with others: Dr. K.-S. Chang guided me on the X-ray, dielectric, and magnetoelectric measurements. M. A. Aronova helped me on the scanning SQUID measurements. Dr. M. Murakami also contributed to the X-ray and scanning SQUID measurements. Dr. M.-H. Yu helped me better understand the results of magnetic measurements. O. O. Famodu and J. Hatrick-Simpers helped with the WDS measurements. Without them, this thesis would not have been possible. I would also like to thank Dr. L. Bendersky of NIST for performing TEM and Dr. C. Gao of the University of Science and Technology of China for giving a great deal of assistance on ferroelectric and magnetoelectric measurements. I would like to acknowledge Neocera Inc. for allowing our group to use their newest scanning SQUID microscope.

Most of all, I would like to thank my family, who gave the most important support during these two years at the University of Maryland, College Park.

Table of Contents

Acknowledgement.....	ii
Table of Contents.....	iv
List of Tables.....	vi
List of Figures.....	vii

Chapter 1 Combinatorial Synthesis

1.1 Introduction to combinatorial synthesis.....	1
1.2 Thin film fabrication.....	4
1.3 Combinatorial thin film synthesis using pulsed laser deposition.....	7
1.3.1 The set up of our pulsed laser deposition system.....	10
1.3.2 The combinatorial pulsed laser deposition flange.....	13
1.4 The techniques to screen combinatorial thin films.....	17

Chapter 2 Exploration of artificial multiferroic thin film using

$\text{PbTiO}_3 - \text{CoFe}_2\text{O}_4$ composition spread

2.1 Magnetoelectric materials.....	20
------------------------------------	----

2.2 Fabrication of PbTiO_3 and CoFe_2O_4 layered composition spreads.....	26
2.2.1 Piezomagnetic material: CoFe_2O_4 (AB_2O_4).....	33
2.2.2 Piezoelectric material: PbTiO_3	34
2.3 Characterization of dielectric properties of PTO-CFO composition spread using scanning microwave microscope.....	36
2.4 Characterization of composition variation across the spreads using wavelength dispersive spectroscopy (WDS).....	42
2.5 Structural phase characterization of PTO-CFO composition spread using X-ray diffractometer (XRD).....	43
2.6 Characterization of magnetic properties of PTO-CFO composition spread.....	50
2.7 Transmission Electron Microscopy of PTO-CFO films.....	59
2.8 Magnetoelectric measurement.....	68
 Chapter 3 Conclusions and future work	
3.1 Conclusions.....	69
3.2 Future work.....	70
 References.....	72

List of Tables

Table 2.1 A set of parameters used to run a program for making 3x (the thickness of pure sides is 3 times of CFO lattice constant) PTO-CFO spread.....	32
---	----

List of Figures

Fig. 1.1	The flow diagram of combinatorial approach to materials.....	2
Fig. 1.2	Relaxed Epitaxy.....	6
Fig. 1.3	Basic set-up of a PLD system.....	9
Fig. 1.4	The combinatorial PLD chamber.....	11
Fig. 1.5	The carousel capable of carrying up to six targets.....	12
Fig. 1.6	Lamda Physics LPX-300 excimer laser.....	13
Fig. 1.7	Pictures of a combinatorial flange. (a) Outside part of the flange. (b) Top view of the vacuum side of the flange.....	15
Fig. 1.8	A schematic top view of the combinatorial flange shutter assembly. (a) Aperture pattern used for discrete libraries. (b) Aperture pattern used for composition spreads.....	16
Fig. 2.1	The triangle shows the coupling of ferroelectricity and ferromagnetism through the mechanical/lattice property of the material to make artificial magnetoelectric composite materials.....	24
Fig. 2.2	(a) Top view of composition spread. (b) Schematic cross section view of a spread sample.....	28

Fig. 2.3	The set up in the chamber for making composition spreads.....	30
Fig. 2.4	The illustration of the shutter moving for the growth of a layered composition spread structure.....	31
Fig. 2.5	Schematic drawing of the spinel structure.....	34
Fig. 2.6	Perovskite structure of PbTiO_3 Pb and O ions constitute a fcc lattice with Ti ions on octahedral interstices.....	35
Fig. 2.7	The schematic drawing of the scanning microwave microscope set up in our laboratory.....	37
Fig. 2.8	Linear dielectric constant measurements on 15x sample (wedge thickness: 12.6 nm).....	40
Fig. 2.9	Non-linear dielectric signal on 15x spread (wedge thickness: 12.6 nm).....	41
Fig. 2.10	Atomic composition distribution versus position on the 15x spread, measured by WDS.....	43
Fig. 2.11	Bruker-AXS scanning X-ray microdiffractor with an automated X-Y stage.....	45
Fig. 2.12	The schematic drawing of diffraction geometry using a 2-D area detector. A range of 2θ and χ are detected simultaneously.....	46
Fig. 2.13	The X-ray microdiffraction at room temperature for 15x spread: the intensity	

	as a function of the 2θ angle and the average composition.....	47
Fig. 2.14	Dielectric constant and D value vs. composition on 15x and 3x spread samples.....	48
Fig. 2.15	(a) X-ray diffraction patterns for pure PTO at different temperatures. (b) The phase transition temperature T_c versus average PTO composition for 15x sample.....	50
Fig. 2.16	The schematic drawing of a scanning SQUID microscope.....	52
Fig. 2.17	(a) Mapping of field emanating from composition spread samples obtained by a scanning SQUID microscope with a standard 15x sample. (b) Mapping of a special spread sample with 5mm pure CFO region at the end.....	54
Fig. 2.18	Field measured by scanning SQUID across composition spreads. The field is due to the in-plane remanent magnetization.....	56
Fig. 2.19	(a) The in-plane and out-of-plane hysteresis loops for pure CFO sample. (b) The in-plane and out-of-plane hysteresis loop for $\text{PTO}_{0.2} - \text{CFO}_{0.8}$ samples.....	57
Fig. 2.20	The non-linear dielectric signal and the in-plane remanent magnetization as a function of composition across the 15x (12.6 nm) composition spread.....	58
Fig. 2.21	Cross sectional TEM of the 15x composition spread taken at approximately	

	PTO _{0.9} – CFO _{0.1} (a) dark field image using g1 vector in (c) (b) dark field image using g2 vector (c) (100) TEM diffraction pattern.....	60
Fig. 2.22	TEM image of PTO _{0.9} – CFO _{0.1} in the 15x spread sample. It shows the twin structures from the tetragonal PTO.....	61
Fig. 2.23	(a) TEM image at the composition PTO _{0.1} – CFO _{0.9} in 15x spread sample. The image is taken along the (110) direction (b) The (100) diffraction pattern. The bright spots belong to CFO, and the darker ones belong to PTO.....	62
Fig. 2.24	(a) TEM image showing the cross section of a PTO _{0.8} – CFO _{0.2} single composition sample. (b) The (100) diffraction pattern showing the reflection spots only belonging to PTO. (c) The (110) diffraction pattern showing the spots only belonging to CFO.....	64
Fig. 2.25	(a) TEM image showing the plane view of a PTO _{0.8} – CFO _{0.2} single composition sample. (b) The (001) diffraction pattern shows the epitaxial relation between the two in this direction.....	65
Fig. 2.26	(a) TEM image of 3x spread sample at composition 0.8PTO-0.2CFO. (b) (100) diffraction pattern. (c) (110) diffraction pattern. From both diffraction patterns, PTO and CFO still keep crystalline.....	67
Fig 3.1	Schematic of a parallel-plate capacitor made with our multiferroic thin	

film.....71

Chapter 1 Combinatorial Synthesis

1.1 Introduction to combinatorial synthesis

The development of computer technology in the recent decades has led to permanent changes in our society. The combination of computers and electronics has contributed to a revolution of automation, and it allows us to perform tasks in a far more efficient way than before. In industry, there is always a demand for high efficiency and better products. From the point of view of materials scientists, this translates to constant and urgent need for materials with better performance in fields such as electronic materials. Thus, there is a need for quick exploration of novel materials. Traditional Edisonian way of discovering materials often cannot meet our need in the rapidly changing world. We need faster, less expensive and better materials exploration techniques in synthesis as well as characterization areas.

Combinatorial synthesis was born in this background. The combinatorial strategy allows one to rapidly fabricate and characterize a large number of different materials. The combinatorial idea was first introduced in the pharmaceutical industry in 1980s in order to speed up the efficiency of drug discovery. Affymax was one of first companies to use combinatorial synthesis to speed up the exploration of catalytic

antibodies. Peter G. Schultz, the founder of Affymax, extended this approach to inorganic materials in 1993 [1,2]. In this approach, a large number of compositionally varying samples are made simultaneously. Rapid screening of the samples is carried out to identify compositions with desirable physical properties. Fig. 1.1 shows one version of a thin film combinatorial synthesis experiment.

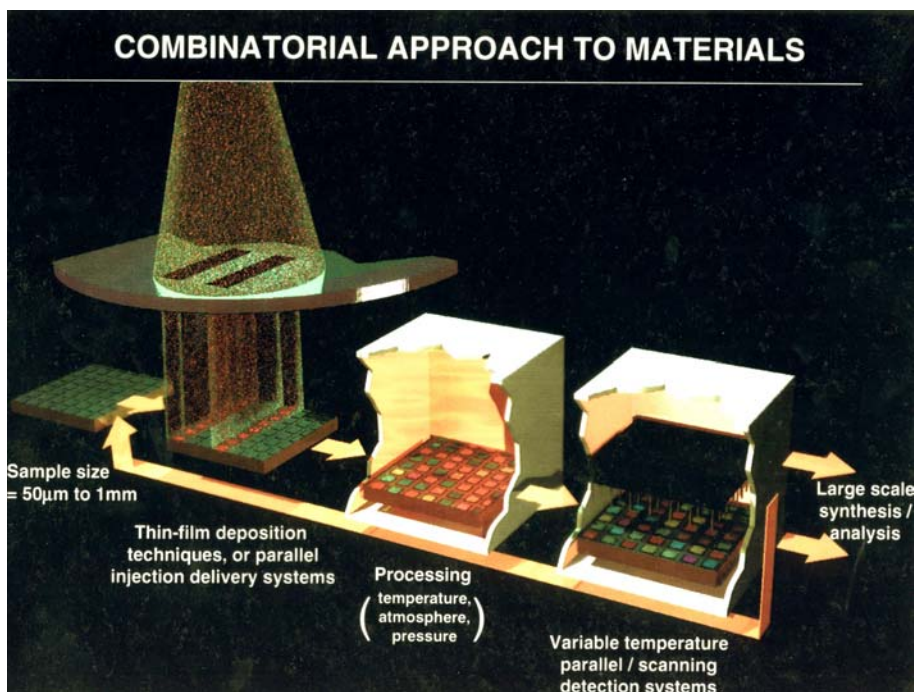


Fig. 1.1 The flow diagram of a thin film combinatorial approach to materials

This thesis focuses on two main steps in combinatorial synthesis experiment: high throughput fabrication and rapid characterization. First, fabrication of samples with

different compositions in a short time is required. High throughput fabrication, which is making samples at a much higher speed than the traditional way, is a main point of combinatorial synthesis. For this purpose, deposition of a composition spread or a discrete library on an individual substrate is performed. In such combinatorial samples, up to thousands of samples can be made simultaneously under the same processing condition. Second, since we have many samples to be examined, rapid measurements of the properties of samples are necessary.

In this thesis, pulsed laser deposition (PLD) was carried out to perform fabrication of composition spreads. Scanning probe microscopes, namely, a scanning microwave microscope and a scanning SQUID microscope were used to perform characterization of the spreads. A scanning X-ray microdiffractometer was used to quickly obtain mapping of phases in the spreads.

At the end of 1980s, it was estimated that there were about 24,000 known inorganic materials, out of which 16,000 were binary compounds and 8,000 were ternary compounds [3]. This seems like a large number, but if we count the number of possible compounds formed by selecting three or four elements randomly from the periodic tables, there are more than 30,000 ternary and 500,000 quaternary compounds, most of which are unexplored. Systematically studying these compounds by the traditional one-by-one

method is simply not practical, and we would never be able to study all the possible compounds. However, if we could employ the combinatorial approach, we can begin to think about studying a large number of compounds rapidly.

There have been combinatorial studies on different classes of materials including superconductors, dielectric/ferroelectric materials, and ferromagnetic materials. We believe that the role of the combinatorial strategy will continue to expand in the future materials research because of its extremely efficient nature. It can speed up the exploration of new materials not only by allowing systematic variation of compositions, but also by enabling variation of processing conditions such as the fabrication temperature.

1.2 Thin film fabrication

Modern semiconductor technology and the electronics industry are largely based on the thin film technology. By depositing thin layers of materials on suitable substrates, materials properties can be reproduced at small scales and in the form which is amenable to making devices.

In the semiconductor industry, epitaxial growth of films, where a single crystal film is coherently deposited on a crystalline substrate, is widely used. There are

two types of epitaxial films: homoepitaxy which refers to the case in which the film and substrate are the same material (ex: Si deposited on a Si wafer), and heteroepitaxy, where a film and a substrate are different materials. Combinatorial synthesis entails growing different materials on different substrates, and thus this is heteroepitaxy. It is well known that materials properties such as magnetic and electrical properties of materials are determined by how the films grow on the substrates.

Due to the mismatch of lattice constants between the materials of interest and the substrate, elastic tensile or compressive stress can be introduced in the film. The strain is relaxed when the thickness is more than the critical thickness (h_c). The critical thickness depends on the difference in lattice constants of the film material and the substrate, and it is proportional to the inverse of misfit strain. Once the film thickness is larger than h_c , dislocations would start to appear at the interface to reduce the stress, and the film gets relaxed. Such case is shown in Fig. 1.2.

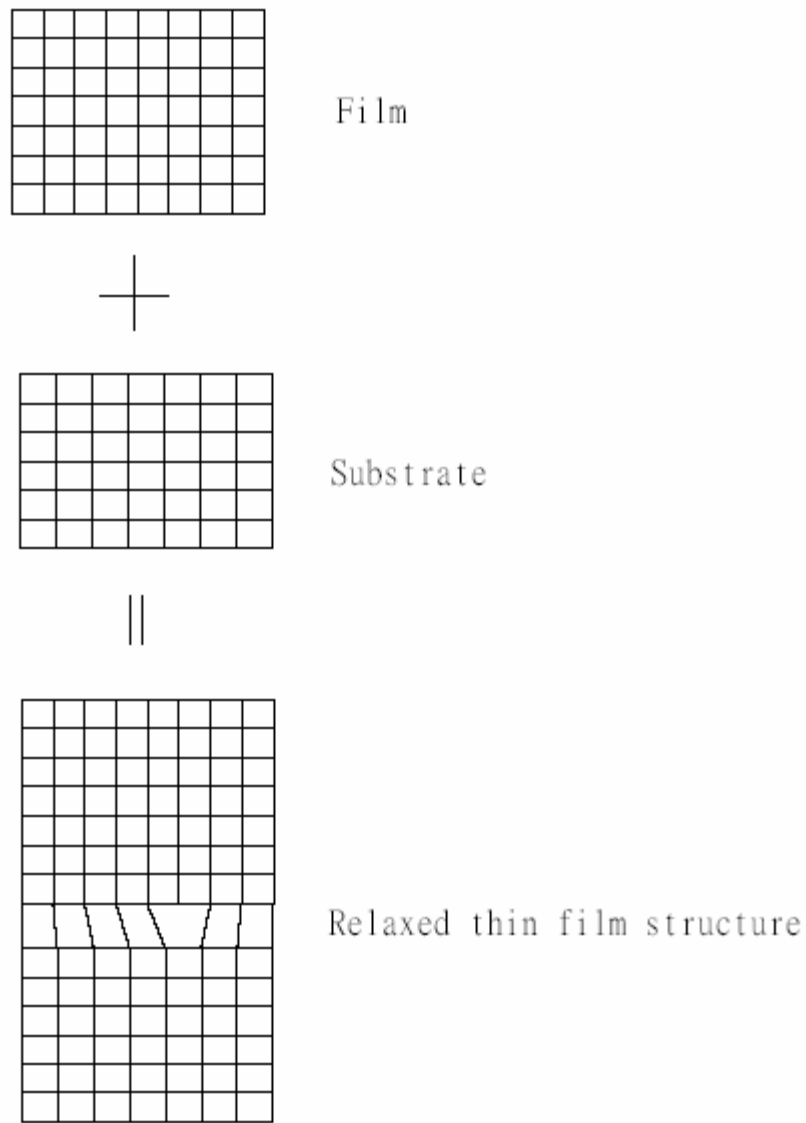


Fig. 1.2 Relaxed Epitaxy

There are three basic modes of thin film growth. These are: (1) Volmer-Weber (island) (2) Frank-Van der Merwe (layer), and (3) Staranski-Krastanov. We discuss these

modes briefly:

- (1) Volmer-Weber (island growth): When the atoms deposited have a stronger bond to each other than to the substrate, they will nucleate to small clusters and grow in islands to three dimensions. This mode most likely happens where there is a significant lattice mismatch between the substrate and the film.
- (2) Frank-Van der Merwe (layer mode): In contrast, if the force between deposited atoms and the substrate is stronger than the bonds between atoms themselves, it results in the layer structure. This mechanism is in 2-D mode.
- (3) Staranski-Krastanov mode: It's possible to have a growth mode in which both of the above mechanisms take place. Because the strain energy increases with the thickness, the layer structure starts to develop into the island growth where dislocations would form to lower the strain energy abruptly above the critical thickness (h_c).

1.3 Combinatorial thin film synthesis using pulsed laser deposition (PLD)

Pulsed laser deposition (PLD) is extensively used in research for metal oxide thin films and devices [4].

The idea of PLD is based on the fact that most nonmetallic materials strongly absorb radiation at ultraviolet range. The laser beam hits the target surface where the laser

energy is converted into thermal, chemical, and mechanical energy to cause target atoms to be ablated from the surface, and the highly directional plasma plume is formed. The plasma plume, containing energetic atoms, molecules, ions, and electrons is highly stoichiometric, which is crucial to making multicomponent metal oxide thin films at different partial pressures. By switching between different targets using a carousel, a variety films and multilayers can be easily made in a single pump-down. Fig. 1.3 shows the basic set-up of a PLD system. A heated substrate is at the other end of plasma plume. The substance ablated from a target is transported to and deposited on the substrate. During and after the deposition, reactive gases such as oxygen or nitrogen are usually injected into the deposition chamber to adjust the stoichiometry of the film.

PLD has several advantages which make it a unique tool among various thin film deposition techniques: (1) it is relatively simple, (2) one can have excellent control of the deposited thickness, and (3) it can produce highly stoichiometric films.

Let us discuss these points:

(1) **Simplicity:** PLD is one of the simplest thin film deposition techniques. From Fig. 1.3, one can see that the basic components of a PLD system are a target holder and a substrate holder in a vacuum chamber.

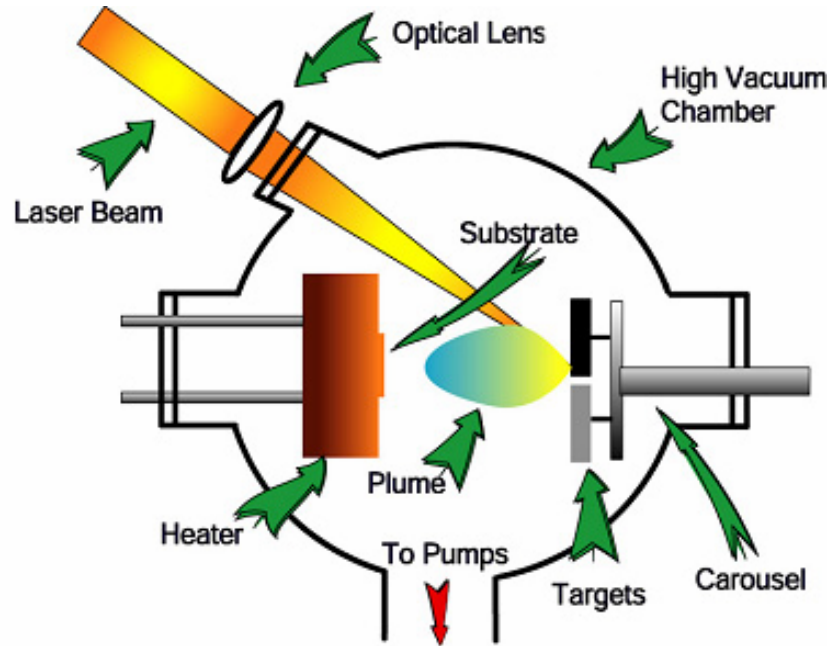


Fig. 1.3 Basic set-up of a PLD system

(2) Excellent control of the thickness of the film: The thickness of a film depends on the amount of materials arriving on the substrate, which is related to the number of the pulses the laser generates. The pulse rate can be changed from 1 Hz to 50 Hz, and the deposition rate in oxide system is typically on the order of $0.1 \text{ \AA}/\text{shot}$ in our system. The thickness of a thin film can be controlled very precisely and easily at nm range by changing the repetition rate and the number of laser pulses.

(3) Highly stoichiometric transfer of materials: Because of the highly non-equilibrium nature of the PLD process, there is good stoichiometric transfer of the target material. The non-equilibrium nature comes from the short pulse duration and the short wavelength of

the laser beam.

The PLD process also has two major disadvantages. First, the uniformity and the limited size of the plume is the major limitation of PLD. Although the size of plume depends on the target material, the laser energy, and the background gas pressure, the typical size of the plume is about 10mm in diameter for our standard oxide deposition condition (O_2 partial pressure: 100 mTorr.). For the target-substrate distance of 10cm, this results in a uniform thickness film in a spot about 10mm in diameter. The highly directional plume results in the gradient of thickness and composition outside of this spot. Second, the macroscopic particulates in the plasma plume from the splash effect, which are enhanced with increasing laser energy, cause the film to have non-smooth surface. The simplest approach to reduce the amount of particulates is to decrease the laser energy and make a rotational target holder. They can be further eliminated by employing advanced techniques such as a velocity selector.

1.3.1 The set-up of our pulsed laser deposition system

The PLD system we are using in our group (shown in Fig. 1.4) is composed of: (1) a vacuum chamber connected to a turbo pump, (2) a carousel capable of carrying up to six targets, (3) a Lamda Physics LPX 300 pulsed excimer laser, and (4) a combinatorial

pulsed laser deposition flange, which I will describe in detail in 1.3.2. The operation of system is managed by a computer program so that it can control the laser pulse rate, the number of shots, switching of the targets, and the shutter motion on the flange to perform spatially selective shadow deposition.

The components are discussed in more details.

(1) The vacuum chamber: A stainless steel chamber connected to a turbo pump can be pumped down to 10^{-7} Torr (Fig. 1.4). The carousel and the flange are mounted on it, and they are taken out for cleaning after every deposition. A UV window, which allows the laser beam to pass through, is also a critical component in the PLD system. The window material, UV grade quartz in our system, needs to be transparent for both visible and ultraviolet light.

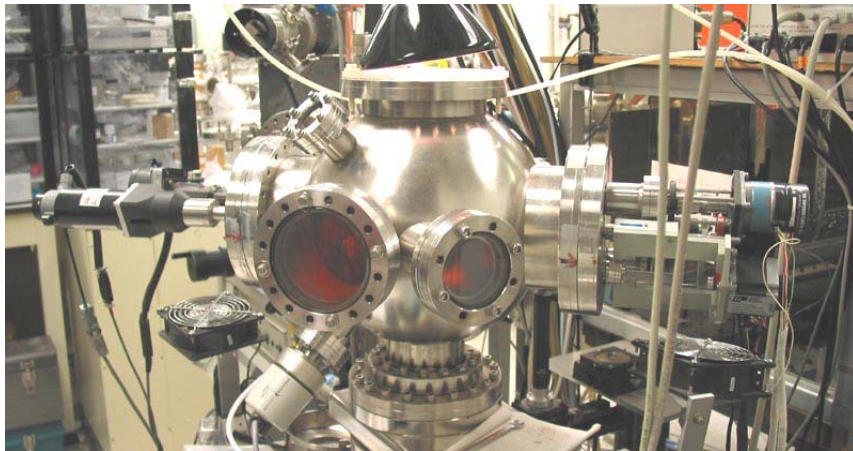


Fig. 1.4 The combinatorial PLD chamber

(2) Carousel: There are six target holders on our carousel (Fig. 1.5) which is driven by two motors connected to the computer. The carousel is used to switch between targets. This allows us to make a multilayer film in a single-run deposition. The carousel also rotates the targets, and the rotation during deposition helps to minimize the generation of macroscopic particulates and maintain a constant deposition rate.

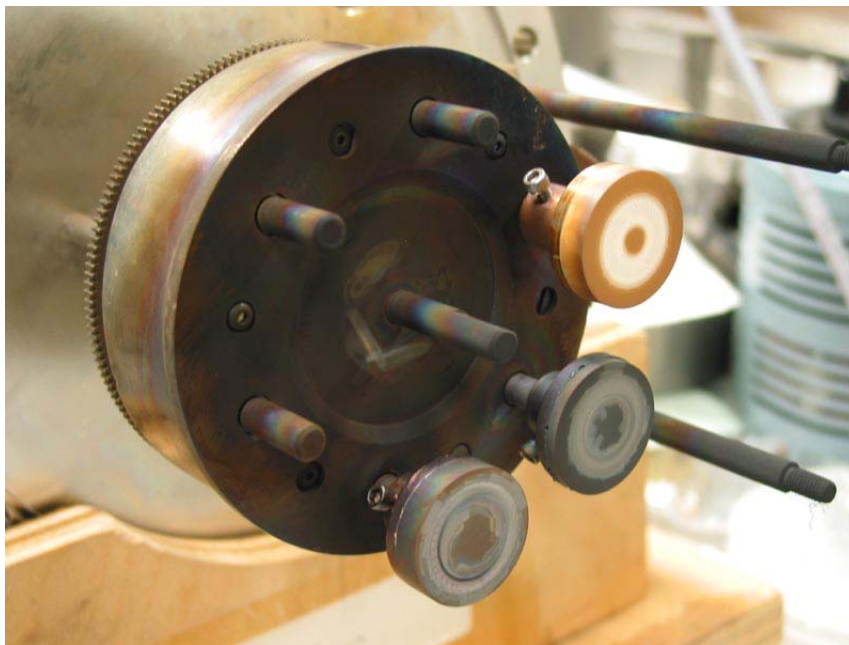


Fig. 1.5 The carousel capable of carrying up to six targets

(3) LPX 300: The Lamda Physics LPX 300 (Fig. 1.6) is an excimer laser with the wavelength of 248nm (KrF). The pulse rate ranges from 1 Hz to 50Hz, and the energy is adjustable from 400 mJ to 1 J. In an excimer laser, excited gases release energy at certain wavelengths. By simply changing the combination of reactive gases, different energies

and wavelengths can be obtained. For example, KrF, ArF, and XeCl are used for 248 nm, 193 nm, and 308 nm, respectively.



Fig. 1.6 Lamda Physics LPX-300 excimer laser

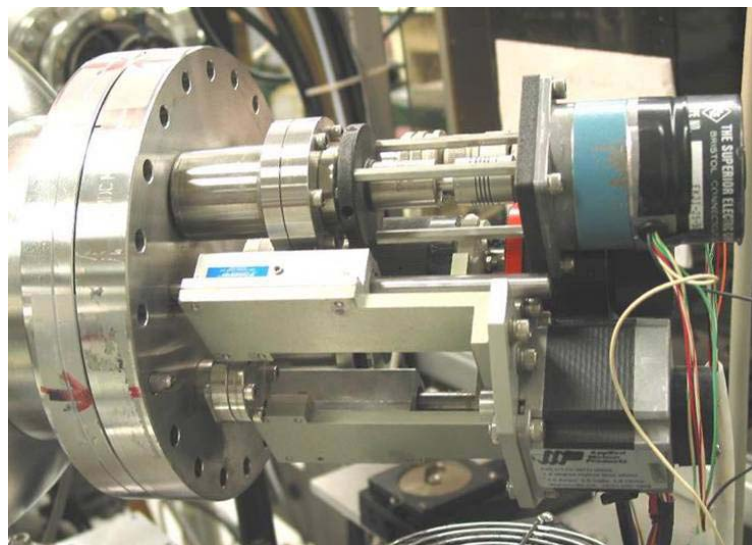
1.3.2 The combinatorial pulsed laser deposition flange

The design of our combinatorial thin-film deposition flange (Fig. 1.7) makes our deposition chamber a very unique PLD system [5]. The flange houses a 1.5-in. diameter sample-mounting heater plate, which can go as high as 800 °C, and a two-dimensional shuttering system, which allows spatially selective deposition on different parts of a substrate. We can use the combinatorial thin-film deposition flange to make a variety of combinatorial libraries and composition spreads. The flange is very compact, and it has

essentially every component we need to perform combinatorial experiments. It is approximately 19 in. in height and weighs 25 lb. We can place it in any PLD chamber with 8 in. flanges. In fact, it can also be used on any physical vapor deposition systems to perform shadow deposition.

The main features of the flange are the feedthroughs and motors which are used to drive the automated shutter system which is controlled by a computer program. The motors are used to rotate chains to which the shutters are connected. The motors are outside the chamber while the chains are inside. The shutter system is a two-axis system, and one shutter moves in the x-direction while the other moves in the y-direction. The shutters are two overlapping steel sheets driven by the chains. The schematic drawing of the shutters is shown in Fig. 1.8.

(a)



(b)

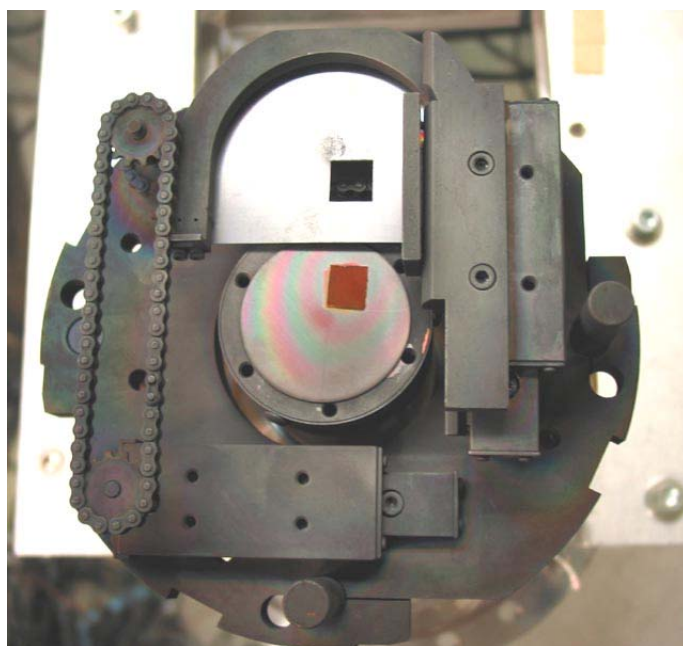


Fig. 1.7 Picture of a combinatorial flange. (a) Outside part of the flange. The feedthroughs are connected to the motors. (b) Top view of the vacuum side of the flange. One shutter with a square aperture is mounted for making composition spreads.

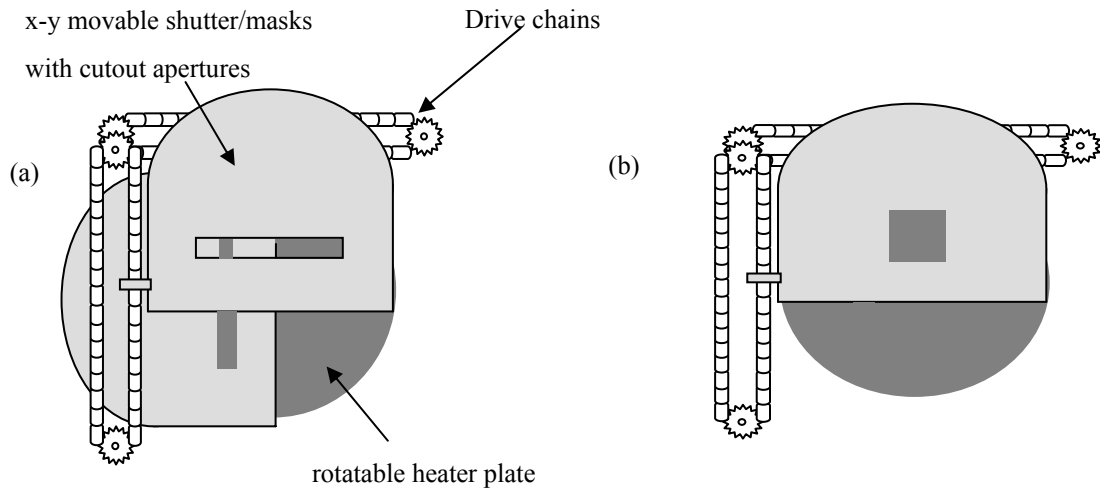


Fig. 1.8 A schematic top view of the combinatorial flange shutter assembly. Masks/shutters and the heater plates are replaceable. Different aperture layouts are used to fabricate different combinatorial libraries or spreads. (a) Aperture pattern used for discrete libraries. (b) Aperture pattern used for composition spreads.

Immediately below the shutter is the heater plate which can be continuously rotated in an automated manner. The distance between the heat plate and the shutter is an important parameter which we need to take into account for deposition at elevated temperatures. It should be long enough to keep the shutter from touching the substrate. At the same time, we would like to bring the shutter as close to the substrate in order to create well-defined shadow deposited features on a substrate. This distance is determined

by the different films making at the different temperatures.

The shutter sheets are replaceable, and a variety of patterns can be cut in the shutters to achieve various shadow deposition geometries. For example, we can make a simple square window to make binary composition spreads. Composition spreads were proven to be an excellent tool for rapidly mapping composition-property phase diagrams [6,7,8,9]. On a binary composition spread, a linearly changing continuous composition gradient is created by moving a shutter during deposition. In particular, two targets, A and B, are ablated by the laser beam, and the ablated materials go through the open aperture on the shutter, which glides over the substrate, resulting in a deposition of a wedge thickness-profiled thin film. The shutter can move at different speeds to allow us to vary the wedge thicknesses. We can control the thickness of each layer to be less than one unit cell. This is used to obtain solid solution of A and B. In contrast, if the thickness is larger than one unit cell, superlattice structures can be obtained. The details of this composition spread fabrication strategy are presented in Chapter 2.

1.4 The techniques to screen combinatorial thin films

One needs to be able to perform rapid screening in combinatorial experiments since many different compositions are made together on a single substrate. Scanning

techniques are very useful for this purpose. We have a scanning X-ray microdiffractometer to obtain structure and phase information. To confirm the actual compositional gradient of spread samples, we use wavelength dispersion spectroscopy (WDS). Scanning superconducting quantum interface device (SQUID) microscopy provides mapping of the magnetic properties. The linear dielectric constant and the non-linear dielectric signals can be obtained from the scanning near-field microwave microscope at microwave frequencies. We also work with Dr. Bendersky in National Institute Standards and Technology to perform transmission electron microscopy (TEM) of our samples.

Chapter 2 Exploration of artificial multiferroic thin films using PbTiO_3 - CoFe_2O_4 composition spread

Artificial multiferroic thin films were explored using composition spreads. Multiferroics are materials that have more than one type of ferroic properties. There are three types of ferroic properties being talked about in this thesis, namely, ferromagnetic, ferroelectric, and ferroelastic properties. Materials with ferromagnetic, ferroelectric, and ferroelastic properties have a spontaneous magnetization, polarization, and deformation, which can be reoriented by the applied magnetic field, electric field, and by applied stress, respectively. In multiferroic materials, at least two of three properties coexist. The coupling between ferroelectricity and ferroelasticity is well known in transducer applications while there are other coupling mechanisms such as the one between ferroelasticity and ferromagnetism is magnetostriction. In this thesis, we focus on artificial magnetoelectric materials, where ferroelectricity and ferromagnetism coexist [10]. In particular, we have studied artificial nanocomposites consisting of PbTiO_3 and CoFe_2O_4 using superlattice composition spreads. A series of superlattice composition spreads were fabricated using our combinatorial thin film synthesis strategy. This thesis focuses on the synthesis of composition spreads of multiferroic thin film

heterostructures consisting of alternating layers of $\text{PbTiO}_3\text{-CoFe}_2\text{O}_4$ and the corresponding measurements are also shown. We have varied the thickness of each layer in different spreads which make up the superlattice. Various measurements were performed on the spreads: scanning microwave microscopy and scanning SQUID microscopy were used to map the dielectric and magnetic properties across the spreads, respectively. We also used the scanning X-ray microdiffractor to characterize the structure and found a phase transition which takes place at certain compositions leading to a maximum in the dielectric constant at these compositions. Wavelength dispersive spectroscopy (WDS) was used to confirm the composition variation across the spreads, and transmission electron microscopy was performed to obtain microstructural information. We have found that the materials actually display a strong departure in microstructural properties from the intended superlattice structures. We have found a range of composition where ferroelectricity and ferromagnetism can coexist.

2.1 Magnetoelectric materials

Magnetoelectricity takes place in a ferroelectric-ferromagnetic multiferroic material where there is a coupling between the two ferroic properties. Such materials can exhibit the magnetoelectric effect where magnetization is modulated by an electric field or the

applied magnetic field causes a change in the electric polarization. This property which comes from the coupling of magnetization and charge polarization can be expressed by Eq. (1) and (2) [11]:

$$P_i = (\chi_e)_{ij} E_j + \alpha_{ij} H_j \quad (1)$$

$$M_i = (\chi_m)_{ij} H_j + (\alpha_{ij}/\mu_0) E_j \quad (2)$$

where P is the polarization.

χ_e is the electric susceptibility.

χ_m is the magnetic susceptibility.

α_{ij} is the magnetoelectric coefficient.

H is the magnetic field.

E is the electric field.

and μ_0 is the magnetic permeability in vacuum.

There are many potential applications of the magnetoelectric effect. Compact and less expensive magnetic-field sensors with high sensitivity can be made by detecting the changes in the electric polarization caused by a varying magnetic field [12]. A new type of memory storage devices is also possible, where data can be written using one

ferroic property and read through another [13].

Unfortunately, there are very few single phase magnetoelectric materials in nature, and the magnetoelectric effect appears to be very weak in these materials. Cr_2O_3 is the first magnetoelectric material discovered by Astrov in 1960, but its magnetoelectric effect is too weak for commercial applications [14]. Even after three decades, there are very few natural magnetoelectric materials. $BiFeO_3$ shows very weak magnetoelectric property based on the thin-film forms instead of bulk materials [15]. $GdMn_2O_5$ single crystals only show the magnetoelectric behavior below 39 K [16]. The contradiction of the general principles of ferromagnetism and ferroelectricity is believed to be the reason that there are so few magnetoelectric materials in nature. 3d-orbital electrons are necessary for creating spin polarization in ferromagnetic materials. However, for most ferroelectric perovskite oxides, there are no 3d-orbital electrons in the B-site atoms because the p-orbital electrons are preferable. This competition between two ferro-properties was illustrated in a first-principle density functional theory (DFT) [13]. It was shown that the off-center distortion essential in ferroelectric materials is reduced by the d-orbital electrons in a transition metal, necessary for ferromagnetism. This indicates that additional driving forces which might come from electrons or lattice is necessary to obtain a useful magnetoelectric property.

Since natural magnetoelectric materials are rare, researchers have tried to make artificial magnetoelectric materials by combining materials with different ferroic properties. Fig. 2.1 is a triangle showing how a magnetoelectric property can be obtained by the product of properties [17]. In artificial magnetoelectric materials, piezoelectric and piezomagnetic properties couple together through the mechanical/lattice property of the material, to cause the magnetoelectric effect. From the way piezoelectric and piezomagnetic properties couple together, we can define the magnetoelectric coefficient

$$\alpha = \frac{\partial e}{\partial H} \cdot \frac{\partial P}{\partial e} \quad (3)$$

where e is the induced strain,

H is the magnetic field

P is the polarization

This shows that the magnetoelectric property can arise from the coupling through induced strain.

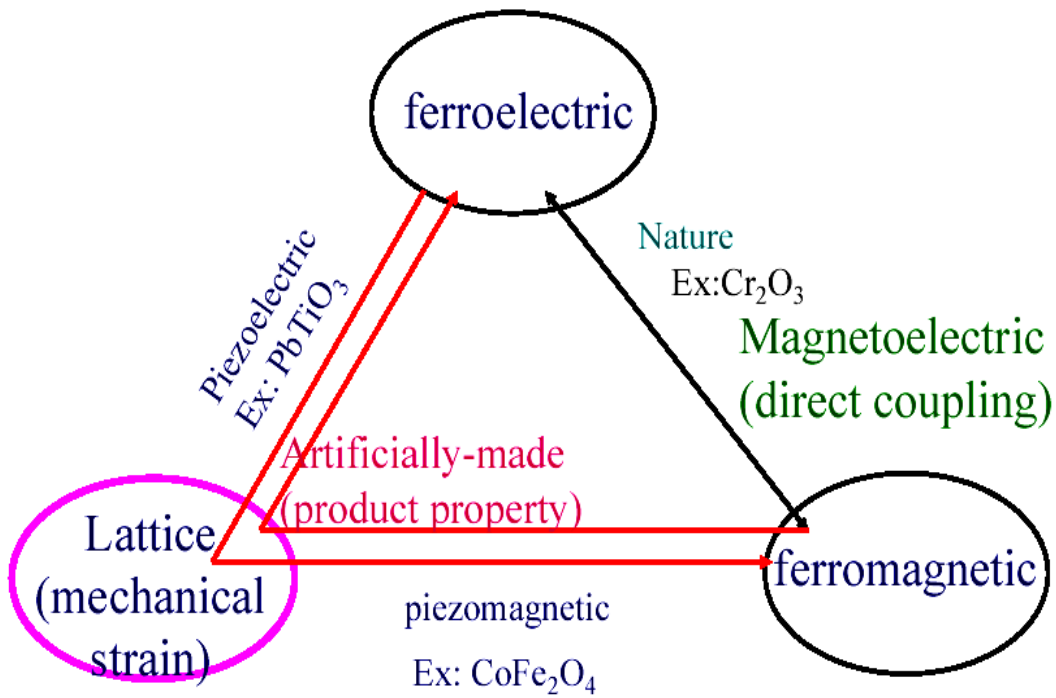


Fig. 2.1 The triangle shows the coupling of ferroelectricity and ferromagnetism through the mechanical/lattice property of the material to make artificial magnetoelectric composite materials.

The first artificial magnetoelectric material was made by J. Van Den Boomgaard by combining a ferroelectric (piezoelectric) BaTiO_3 and a ferromagnetic (piezomagnetic) CoFe_2O_4 in a eutectic sintered composite [18, 19, 20, 21]. The magnetoelectric coefficient α from this experiment was $0.13 \text{ V}/(\text{cm} \times \text{Oe})$ which was far below that predicted from the theoretical calculation ($5 \text{ V}/(\text{cm} \times \text{Oe})$) [22]. The reason for

the low value might be the unfavorable phases which were formed at a high fabrication temperature over 1000 °C.

Researchers turned to make layered composites to eliminate this drawback. To enhance the magnetoelectric effect, Harshé *et al* proposed to use epoxy to create the bilayered or multilayered composite structures. [13]. There are two advantages to making layered composites instead bulk eutectic: First, the piezoelectricity can be improved due to the ease of poling of the piezoelectric layers. In addition, the piezoelectric property is well separated from the piezomagnetic layers. Many magnetoelectric materials based on layered structures have been reported. These include composite of (Pb,Zr)TiO₃ (PZT) – Tb_{0.3}Dy_{0.7}Fe_{1.92} (Terfenol-D), PZT-NiFeO₄, Polyvinylidene fluoride (PVDF) – Terfenol-D, laminate Pb(Mg_{1/3}Nb_{2/3})O₃ – PbTiO₃ (PMN-PT) – Terfenol-D, PZT – FeCoSiB, PZT – CoFe₂O₄, PZT – (La,Sr)MnO₃, PZT – (La,Ca)MnO₃ and BaTiO₃ (BTO) – BiFeO₃ [23, 24, 25].

These results are all based on bulk materials. Our research in this thesis focuses on the properties of layered thin films.

2.2 Fabrication of PbTiO_3 (PTO) and CoFe_2O_4 (CFO) layered thin film composition spreads

Almost all research on artificial magnetoelectric materials at present time are focusing on bulk composites. Even the layer-structured composites are in bulk forms. Thin film heterostructures provide a new configuration to explore this property and advantages over bulk: 1) layered structures can be used to control the thickness of alternating piezoelectric and pieomagnetic layers at nanometer scale; 2) thin film devices based on the magnetoelectric property can be investigated.

There are several requirements for the materials we are using to synthesize the layered structures: 1) the ferromagnetic material needs to be the insulator and has high magnetostriction, 2) the ferroelectric material needs to have a high piezoelectric coefficient. Based on these reasons, we selected PbTiO_3 (PTO) as the ferroelectric material and CoFe_2O_4 (CFO) as the ferromagnetic material.

We use our combinatorial PLD technique to make PTO-CFO composition spread samples in which the average composition changed continuously from pure PTO to pure CFO so that we can investigate the changing physical properties as well as coupling as a function of average composition.

The composition variation takes place in 6 mm. At both ends of the spreads,

there are 2 mm of pure end composition which can provide a reference in measurements.

Fig. 2.2 shows the top view and a cross section schematic of a spread sample.

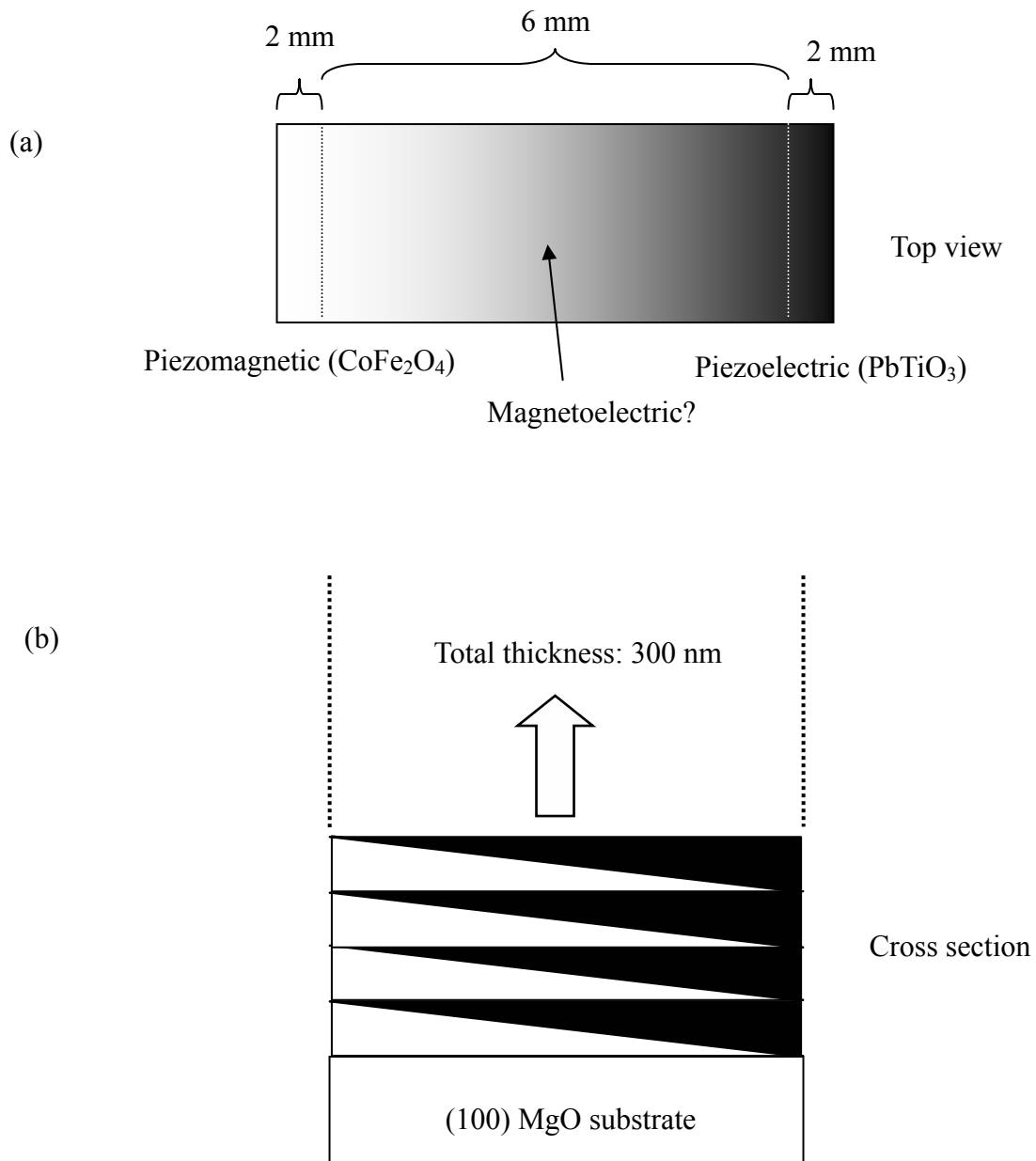


Fig. 2.2 (a) Top view of composition spread. There is a 2mm pure PTO and a 2mm pure CFO end on each side. The average composition is continuously changing over 6mm from one end to the other. (b) Schematic cross section view of a spread sample.

All samples are grown on 10mm x 10mm (001) magnesium oxide (MgO, cubic with $a=0.42$ nm) substrates at $600\text{ }^{\circ}\text{C}$. CFO has a cubic structure with a lattice constant $a=0.839$ nm, and PTO has a tetragonal structure with $a= 0.39$ nm and $c= 0.42$ nm. Although these materials have different structures, the mismatch between twice the lattice constant of PTO and the lattice constant of CFO is around 5%, and we found they can be grown together heteroepitaxially on (001) MgO substrates. CFO and PTO targets are ablated by a KrF (248 nm) excimer laser. The oxygen partial pressure during the deposition was 65 mTorr.

A number of PTO- CFO composition spread samples were made. They were made to be superlattice composition spreads and there was more than one unit cell of PTO and CFO at the two ends of each wedge layer. This was done to ensure some integrity in properties of the respective materials since PTO and CFO are not known to form a solid solution.

The total thickness of a spread film is fixed at 300 nm across the spread. For synthesizing the spreads, a single shutter with a square window as shown in Fig. 1.10 (b) is used, and the deposition set up in the chamber is as shown in Fig. 2.3. Fig. 2.4 illustrates the relation between laser pulses, shutter motion, and the growth of CFO and PTO. In this figure, the shutter is moving to the left when PTO target is ablated by the

laser to grow wedge-like PTO layers, and it is moving back to the right when the CFO target is ablated to make wedge-like CFO layers.

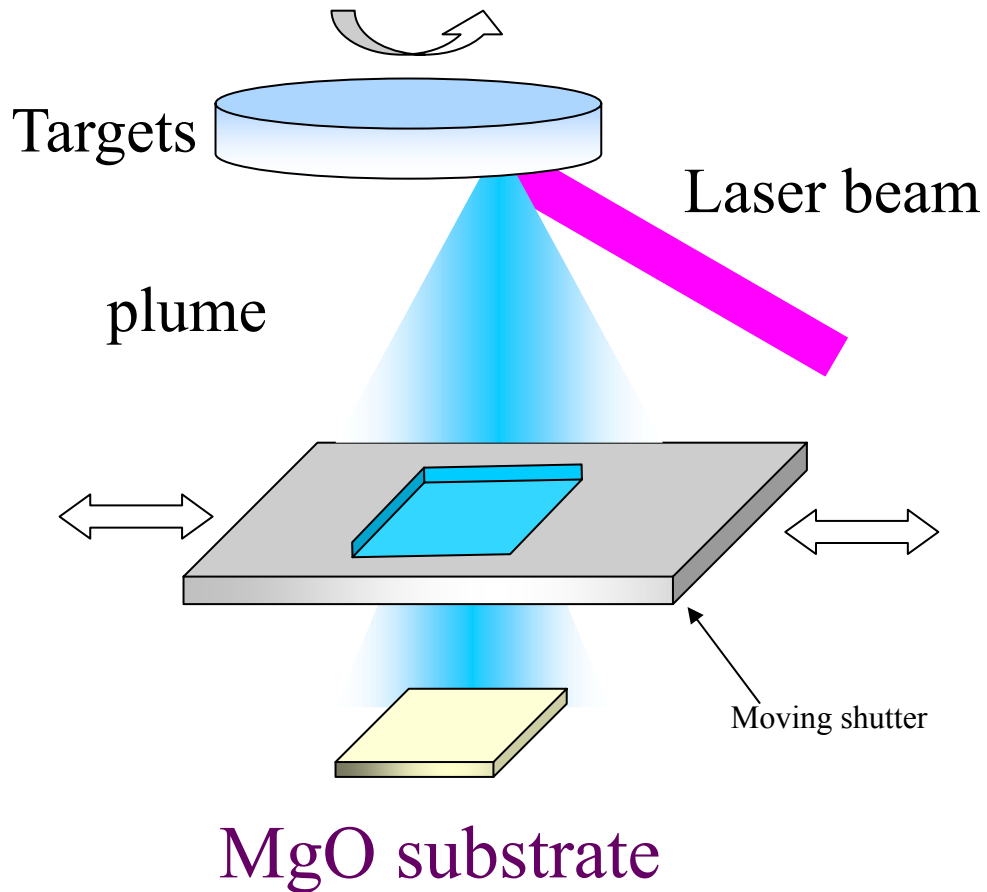


Fig. 2.3 The set up in the chamber for making composition spreads. The shutter with a single square window is moving back and forth as targets are ablated.

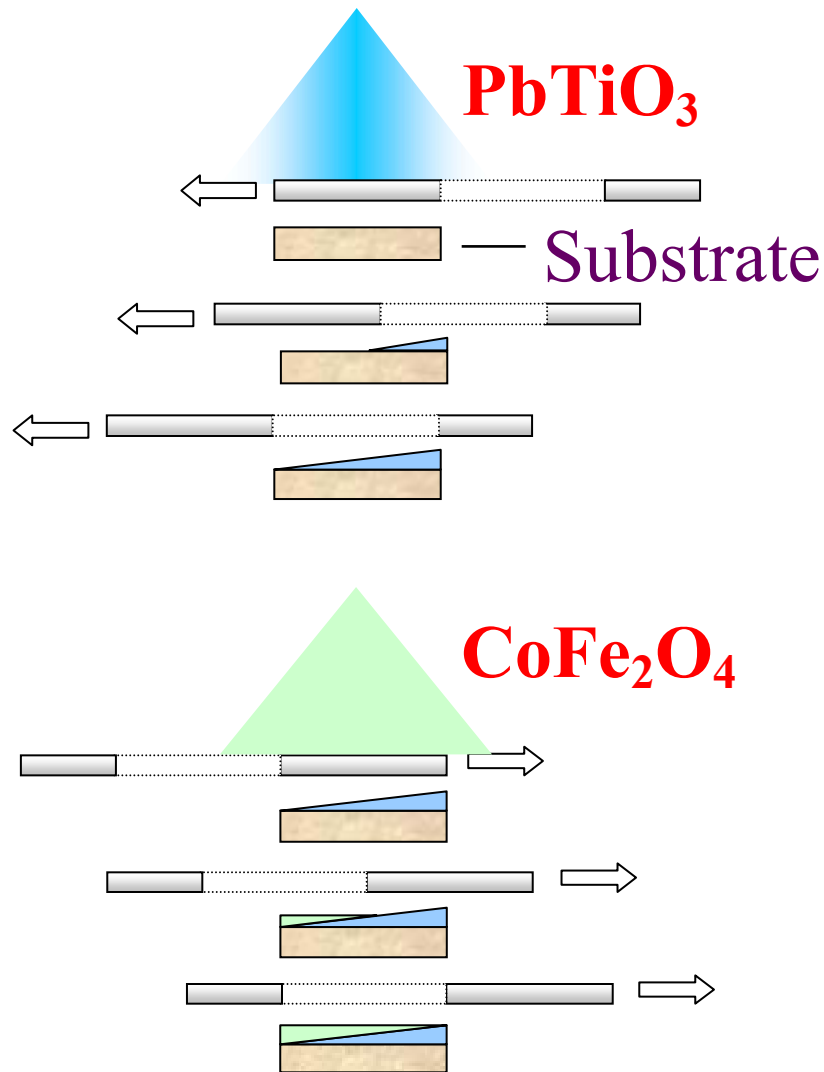


Fig. 2.4 The illustration of the shutter motion for the growth of a layered composition spread structure. The shutter is moving to the left when the PTO target is ablated while it is moving to the right for the growth of CFO layers.

In our PLD system, the thickness of each layer is controlled by several parameters: shutter motion speed, the laser pulse rate, and the total number of laser pulses. Below

shows an example of the parameters used in one cycle to make a spread sample.

Shutter motion sequence no.	Target	Motor speed (rpm)	Shutter moving distance (mm)	Laser pulse rate (Hz)	Number of laser shots
1	PTO	200	-6	8	39
2	None	500	-10	0	0
3	CFO	100	6	20	195
4	None	500	10	0	0

Table 2.1 A set of parameters used to run a program for making 3x (the thickness of each wedge layer is 3 times of CFO lattice constant) PTO-CFO spread. Each sequence number includes one set of parameters in the computer program. Sequence number 1 and 3 are where PTO and CFO wedge layers are deposited, respectively. Sequence number 2 and 4 are where the shutter gets reset. In this 3x spread, the computer program will repeat this procedure for 119 cycles to make the film 300 nm thick everywhere.

Due to the different deposition rates for CFO and PTO targets, the deposition time and the laser pulse rate are different for each target even if their wedge thickness is to be

the same. In the computer program, we use the shutter speed to control the deposition time which, together with laser pulse rate is used, to control the thickness of one wedge layer. Between the depositions of two targets, we need sequences of shutter motion in order to set the shutter at the starting point for the next deposition.

The total thickness of the spread film is 300 nm everywhere in the sample while the thickness of each wedge layer was varied from one to multiple unite cells. A series of composition spreads were made where the thick end of each wedge layer for both CFO and PTO was approximately 0.84 nm, 2.52 nm, 5.04 nm, 8.4 nm, and 12.6 nm which correspond to 1x, 3x,10x, and 15x the unite cell of CFO, respectively.

2.2.1 Piezomagnetic material: CoFe_2O_4 (AB_2O_4)

CoFe_2O_4 has a very complicated structure. It has the spinel ferrite structure with a stoichiometry denoted by AB_2O_4 , where A is a divalent transition metal ion or a mixture of a trivalent and a monovalent metal ion. A spinel is basically a cubic structure in which O^{2-} ions form an fcc lattice. It requires eight formula equivalent AB_2O_4 to form a repeating unit cell which contains 32 O^{2-} ions, 64 tetragonal sites (A sites) and 32 octahedral sites (B sites). However, only 8 tetragonal and 16 octahedral sites are occupied so that the ratio of the number of atoms between A atoms and B atoms is 1:2.

Fig. 2.5 is a schematic drawing of the spinel structure.

CFO is known to have highly anisotropic magnetic properties and has been widely used in magnetic media and microwave device applications. It has been reported that the easy axis of an CFO epitaxial thin film grown on a (001) MgO substrate is out of plane [26].

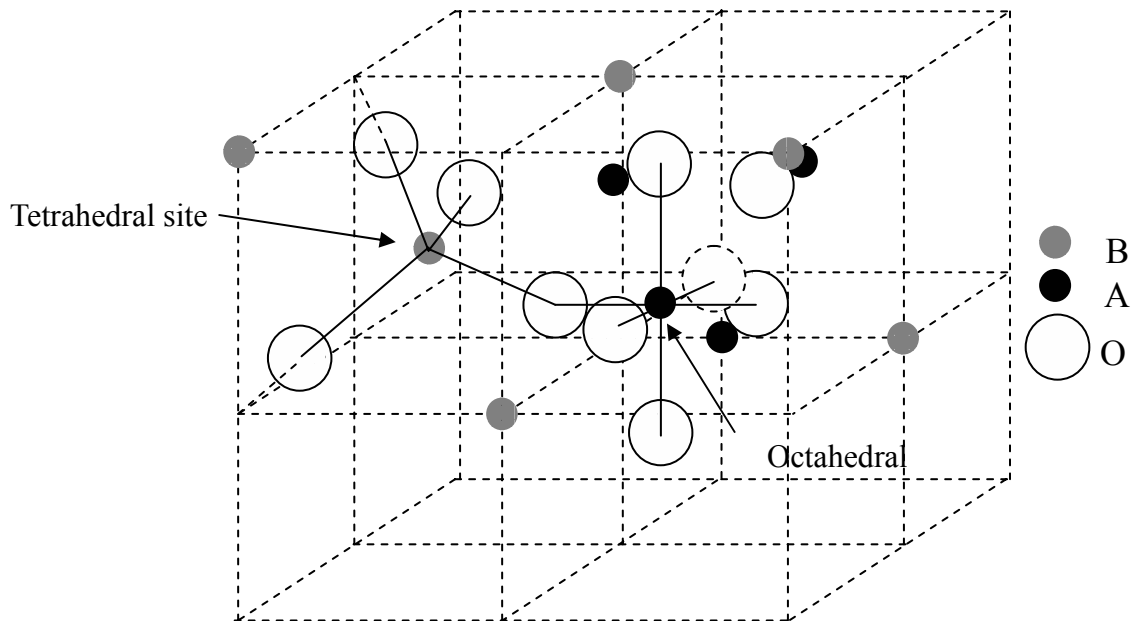


Fig. 2.5 Schematic drawing of the spinel structure [27]

2.2.2 Piezoelectric material: PbTiO_3

PbTiO_3 (PTO) is a perovskite in which Ti ions are surrounded by six oxygen ions in octahedral sites. Pb and O ions constitute an fcc lattice with Ti ions on octahedral

interstices as shown in Fig. 2.6. At temperatures higher than the ferroelectric T_c , PTO has a cubic structure while it becomes tetragonal with the Ti ion in an off-center position to give rise spontaneous polarization below T_c . In ferroelectric materials, there exists a domain structure, which is similar to ferromagnetic materials, with a net spontaneous polarization in the domain.

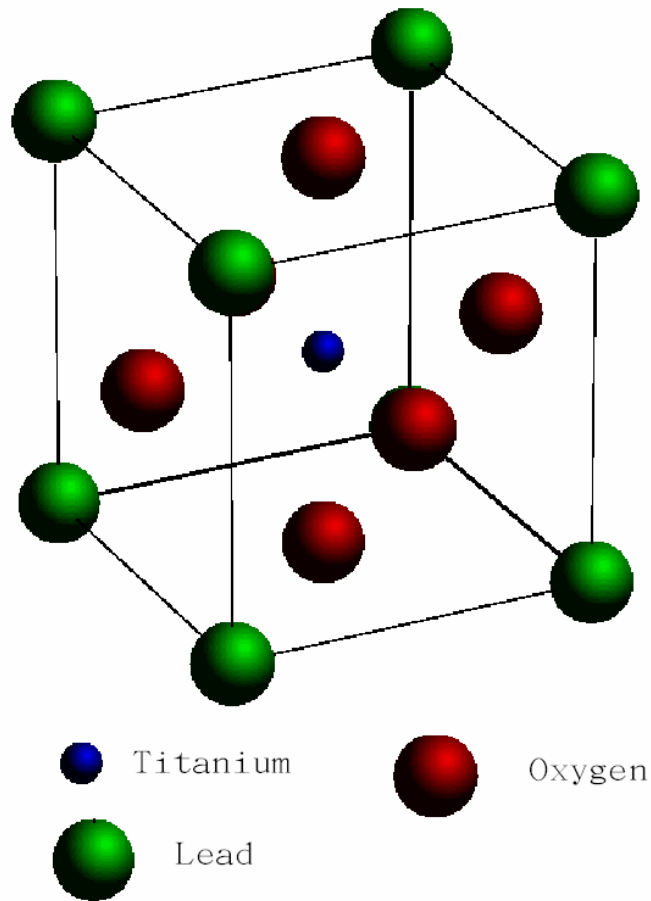


Fig. 2.6 Perovskite structure of PbTiO_3 Pb and O ions constitute a fcc lattice with Ti ions on octahedral interstices

2.3 Characterization of dielectric properties of PTO-CFO composition spreads

In this experiment, we use the near-field scanning microwave microscope to map the dielectric property on the spread samples (Fig. 2.7). The near-field microwave microscopy has been proven to be a powerful, non-destructive tool for mapping microwave dielectric properties of combinatorial samples with high spatial resolution [28, 29, 30]. Due to the fact that the propagating electromagnetic wave can't carry information smaller than the wavelength λ , the only two ways to improve the resolution is either to use a higher energy source to get a shorter wavelength, or to use the near-field technique. The concept of near-field is that a very small object can be detected if it is placed very close to the light source. We use a tip-structure scanning microwave probe for the near-field microwave microscopy. This microscope has been demonstrated as an ideal tool for combinatorial samples since it provides rapid and non-destructive measurement with the very high resolution (down to sub μm) [31, 32]. Figure 2.7 shows the basic set-up of this microwave microscope. It is composed of a high- Q $\lambda/4$ coaxial cavity with an STM tip mounted to the center conductor, which protrudes through an aperture in the bottom plate. The tip will be brought very close to the sample to do the measurement. By measuring the shift of Q and the resonant frequency, we can calculate the dielectric constant by applying the perturbation theory.

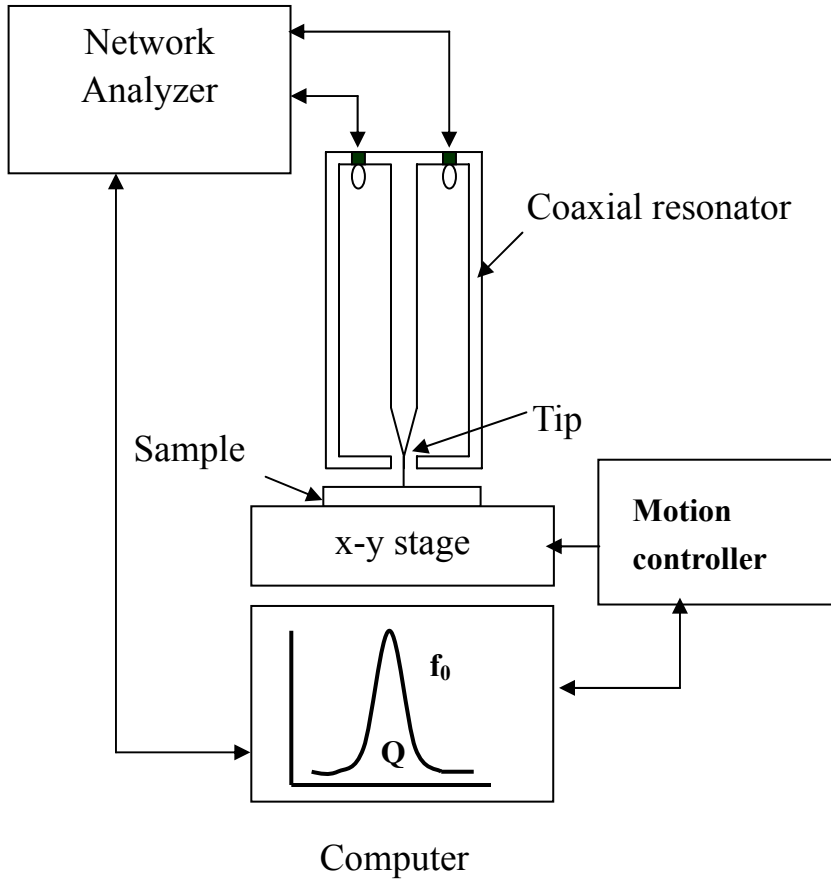


Fig. 2.7 The schematic drawing of the scanning microwave microscope in our laboratory.

In addition to the linear dielectric constant, the non-linear dielectric signal, which is proportional to the non-linear dielectric constant, can also be measured with this microwave microscope by applying an electric field on the sample. The non-linear dielectric constant is the tunable part of the dielectric constant, and thus it is a direct indication of ferroelectricity. It changes with the applied electric field.

The general relationship between the electric displacement D, the polarization P, and the applied electric field E can be written as:

$$D_i = P_i + \sum_j E_j (\epsilon_{ij} + \sum_k \epsilon_{ijk} E_k + \dots) \quad (1)$$

where D is the displacement, P is the polarization.

E is the electric field.

ϵ_{ij} is the second order dielectric constant.

and ϵ_{ijk} is the third order dielectric constant.

The effective dielectric constant ϵ_{eff} (Eq. (2)) is defined as the derivative of displacement with the electric field.

$$\epsilon_{\text{eff}} = \partial D_i / \partial E_j = \epsilon_{ij} + \sum_k \epsilon_{ijk} E_k + \dots \quad (2)$$

In Eq (2), ϵ_{ij} is the linear part of dielectric constant, and the others are higher order terms.

The 1st order non-linear dielectric signal ϵ_{ijk} can be extracted as the difference between the total effective dielectric constant and the linear dielectric constant (eq. (2)) while applying an electric field to the sample. The non-linear signal we can measure is usually the 1st order non-linear dielectric signal ϵ_{ijk} . The higher order terms are negligible small.

A signal generator is used to apply a low frequency oscillating voltage (1 KHz, 16V)

between the microscope tip and a metallic electrode on the back side of the sample substrate to modulate the effective dielectric constant of the sample.

Linear dielectric constant measurements at 1GHz on 15x spread sample (wedge thickness: 12.6 nm) are shown in Fig. 2.8. The measurement is taken as a function of the position and consequently a function of the average composition on the sample. The general trend is that the dielectric constant decreases toward the CFO end. In all spreads, we observe a peak in the dielectric constant at composition away from the pure PTO end, and here we take the 15x sample as a representation.

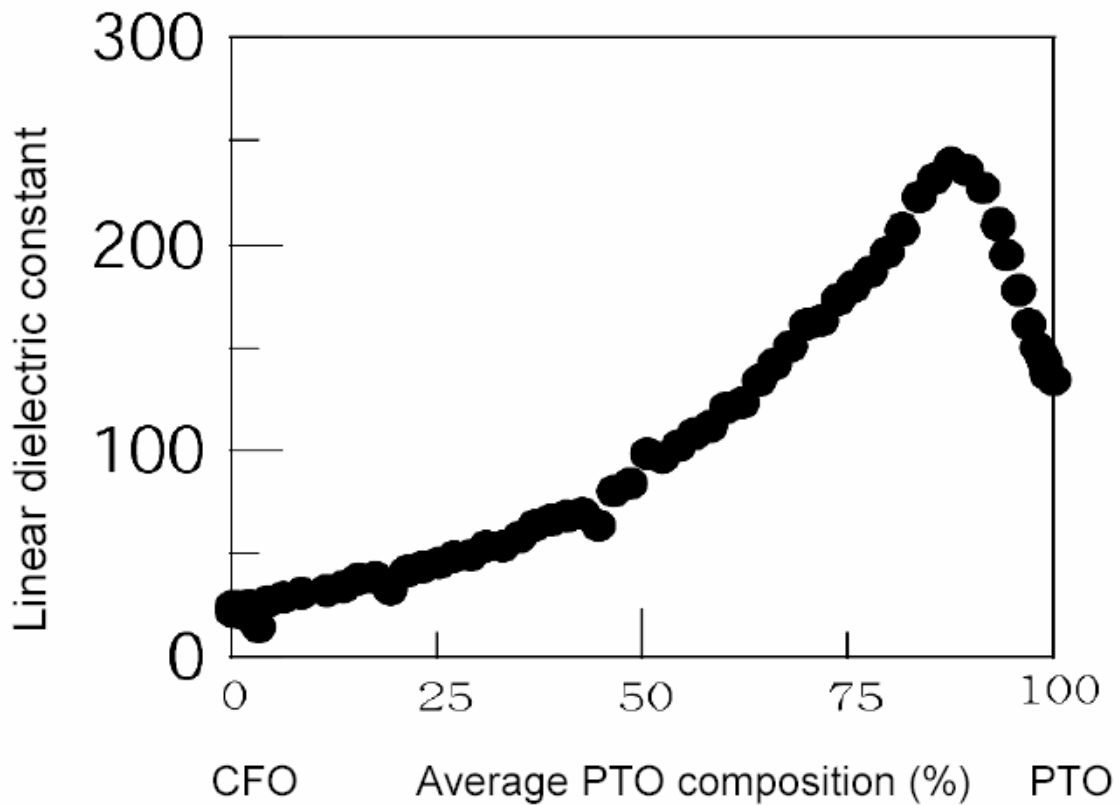


Fig. 2.8 Linear dielectric constant measurements on 15x sample (wedge thickness: 12.6 nm). There is a peak for the dielectric constant around composition at (PTO)_{0.85}-CFO_{0.15}.

We also measured the non-linear dielectric signal across the spreads. The peaks are even more evident in the non-linear dielectric measurement, and it seems that the peaks occur at the same composition as the linear dielectric constant near the average composition of (PTO)_{0.85}-CFO_{0.15}. No non-linear signal was observed in the 1x sample.

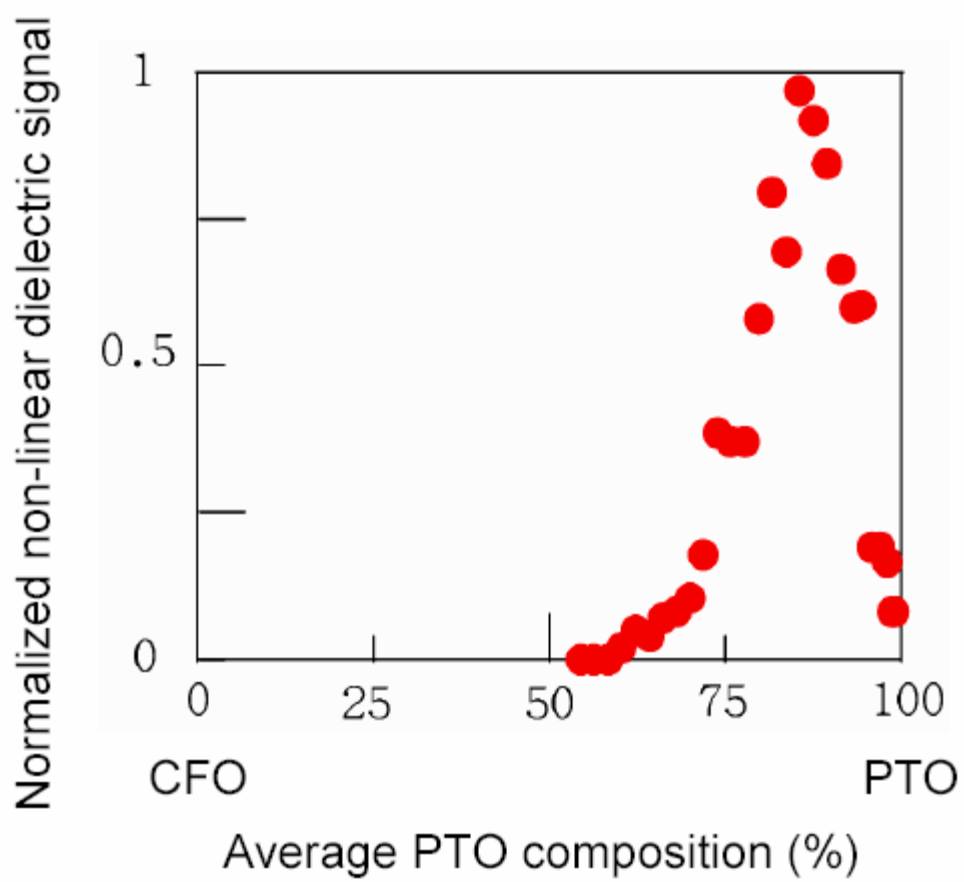


Fig. 2.9 Non-linear dielectric signal on 15x spread (wedge thickness: 12.6 nm).

2.4 Characterization of composition variation across the spreads using Wavelength dispersive spectroscopy (WDS)

Wavelength dispersive spectroscopy (WDS) is a widely used tool for determining compositions of materials. Unlike energy dispersive spectroscopy (EDS) which collects all energy distribution at once to show a histogram of counts versus energy, in this technique, individual wavelengths are detected at different points on the Rowland circle by coupling the motion of a sample and the detector in WDS. Both techniques detect the emitted X-ray from a sample upon electron beam irradiation. Compared to EDS, WDS provides a higher resolution due to its better ability to separate wavelength peaks.

In our experiment, WDS was used as an effective tool to verify the composition variation across the spreads. Fig. 2.10 shows the atomic mole ratio as a function of position on a 15x spread sample. It shows that the composition variation in the spread is approximately as we designed it to be, and the composition varies linearly.

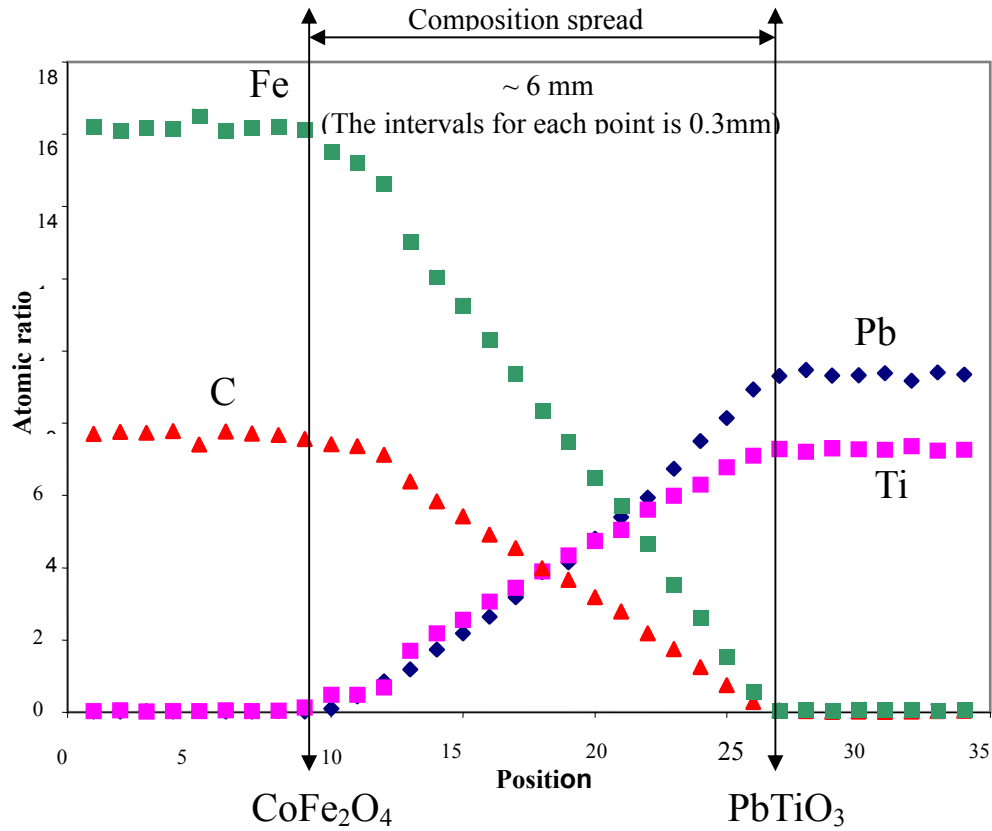


Fig. 2.10 Atomic composition distribution versus position on the 15x spread, measured by WDS.

2.5 Structural phase characterization of PTO-CFO composition spread using X-ray diffractometer (XRD)

Fig. 2.11 shows the scanning X-ray microdiffractometer we use to determine the structure in materials. It is a D8 DISCOVER with GADDS by Bruker-AXS, equipped with a two-dimensional (2-D) area detector (diameter: 11.5 cm) and an x-y-z stage for combinatorial screening to characterize the out-of-plane lattice constant of the film across

the spread samples. The most important features of this tool are the automated X-Y stage which allows us to scan many points at once, and the two-dimensional area detector. Fig. 2.12 shows the detection schematic of this diffractometer. In contrast to the traditional point detector which can only detect the diffracted beams in the detection plane, the 2-D area detector can pick up the signals at certain angle range along the Z-direction in Fig. 2.12, which contain the χ information. This operational mode, which is called the ω scan, is very useful to study epitaxial films. If the sample is polycrystalline, the diffracted beams will form a cone in the 3-d space. This cone will intersect with the plane on the area detector to form a ring while on a point detector it would only give a spot. If the sample is a single crystal, it would give a spot.

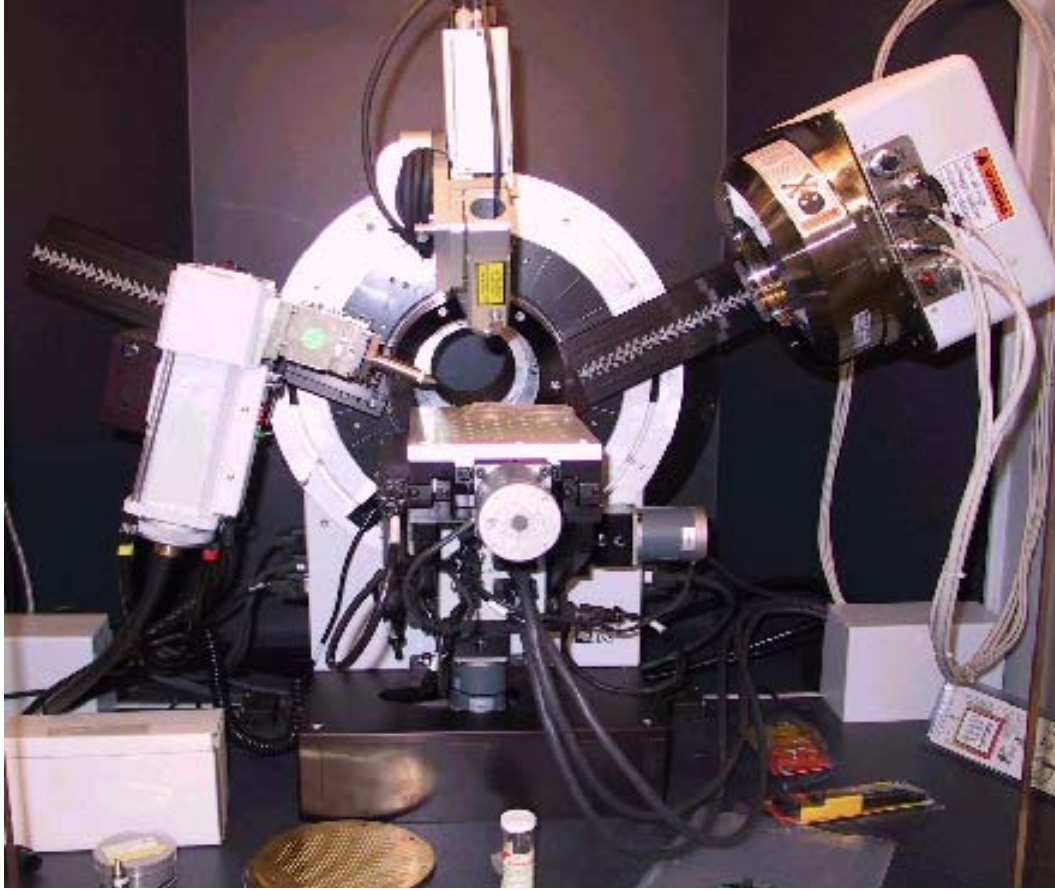


Fig. 2.11 Bruker-AXS scanning X-ray microdiffractor with an automated X-Y stage. The area detector is on the right.

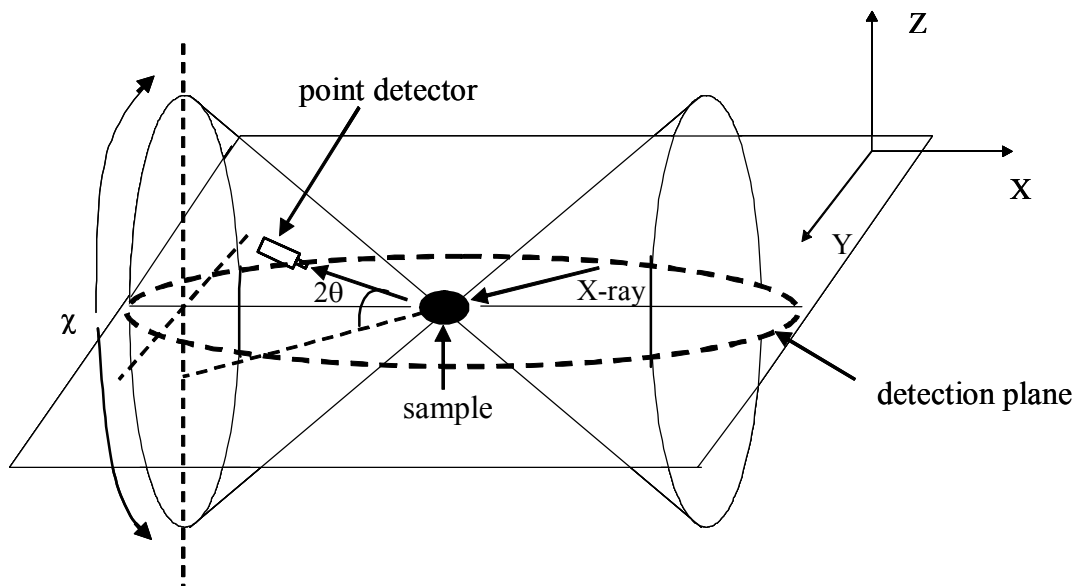


Fig. 2.12 The schematic drawing of the diffraction geometry using a 2-D area detector. A range of 2θ and χ are detected simultaneously.

In order to understand the unexpected peak behavior in dielectric properties at composition away from the pure PTO end in our spreads, a phase evolution measurement was carried out using the scanning X-ray microdiffractometer. Fig. 2.13 shows the result for 15x sample, where the intensity is plotted as a function of the average composition and the 2θ angle. The (002) and (200) tetragonal-PTO peaks gradually merge together to become the (200) cubic PTO peak around the composition of $(\text{PTO})_{0.85} - (\text{CFO})_{0.15}$ with increasing CFO content from the PTO end. Thus, we can associate the highest linear dielectric constant and the non-linear dielectric signal to the phase transition between

tetragonal and cubic phases.

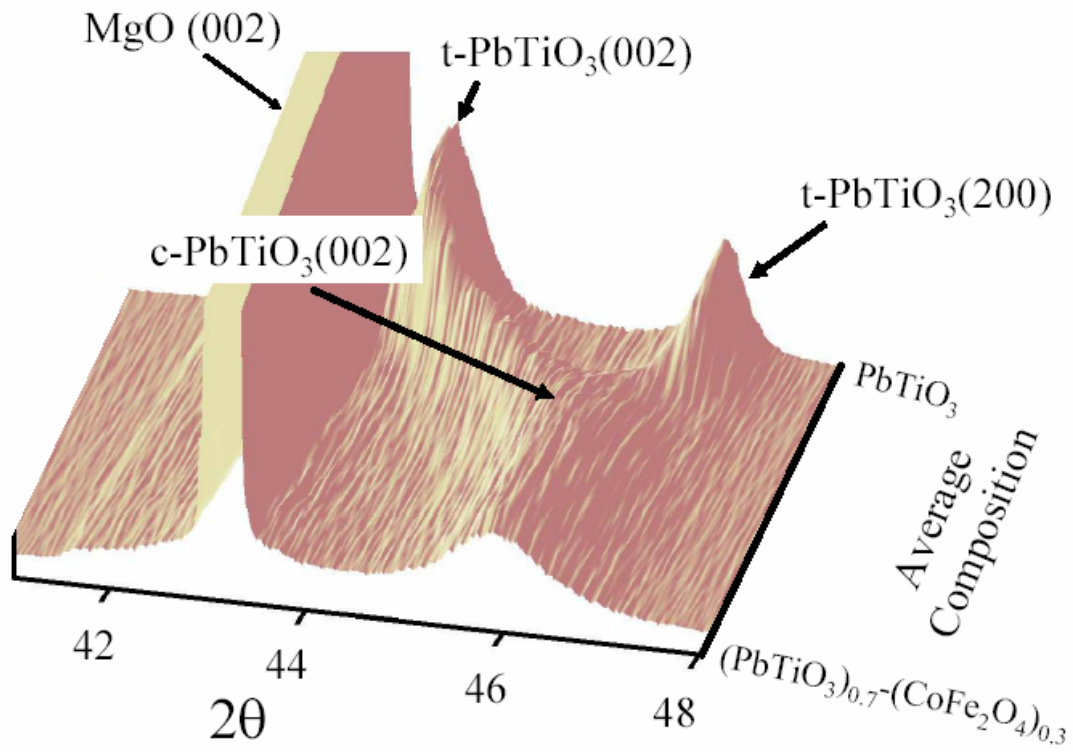


Fig. 2.13 The X-ray microdiffraction at room temperature for 15x sample: the intensity as a function of the 2θ angle and the average composition. The phase transition from the tetragonal-PTO to the cubic-PTO occurs at the average composition of $(\text{PTO})_{0.8} - (\text{CFO})_{0.2}$.

We plot the linear dielectric constant, the non-linear dielectric signal, and d-value variation (calculated from the diffraction data) together to clearly illustrate the relation between the dielectric constant properties and the phase transition in Fig. 2.14.

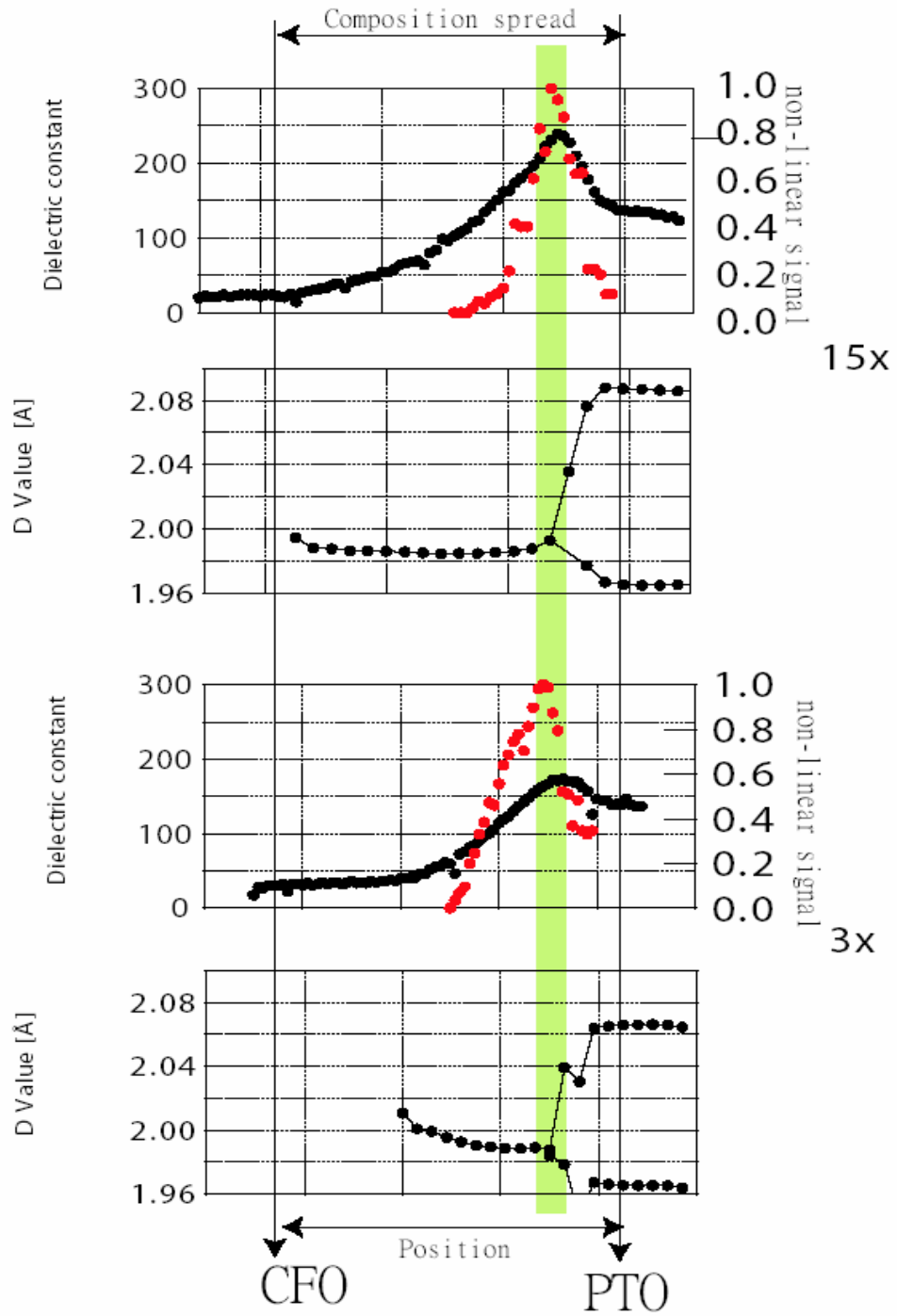


Fig. 2.14 Dielectric constant and the d value vs. composition on 15x and 3x spread samples. The positions of the dielectric peaks correspond to the PTO ferroelectric transition. The d value is half the lattice constant for PTO calculated from X-ray result.

In addition, the temperature-dependent phase evolution can be carried using the temperature stage of the diffractometer. Since the ferroelectric phase transition happens at ferroelectric T_c , the temperature-dependent X-ray measurements on spread sample can give us the relation between composition and T_c . Fig. 2.15 (a) shows how we determine T_c . It shows one set of X-ray diffraction patterns at different temperatures. The two peaks belonging to the tetragonal phase gradually merge into one peak belonging to the cubic PTO. We assume that the temperature at which the two peaks of the tetragonal phase merge into one peak of the cubic phase is the ferroelectric phase transition temperature. Fig 2.15 (b) shows the phase transition temperatures (T_c) versus composition from the room temperature to 600 °C for several compositions from the 15x sample. From the measurement, T_c of pure PTO is about 510 °C which is consistent with the bulk data. With increasing CFO content, T_c is brought down, and it goes to the room temperature at the composition around $(\text{PTO})_{0.85} - (\text{CFO})_{0.15}$. This indicates that the T_c is tunable by controlling the content of CFO into PTO.

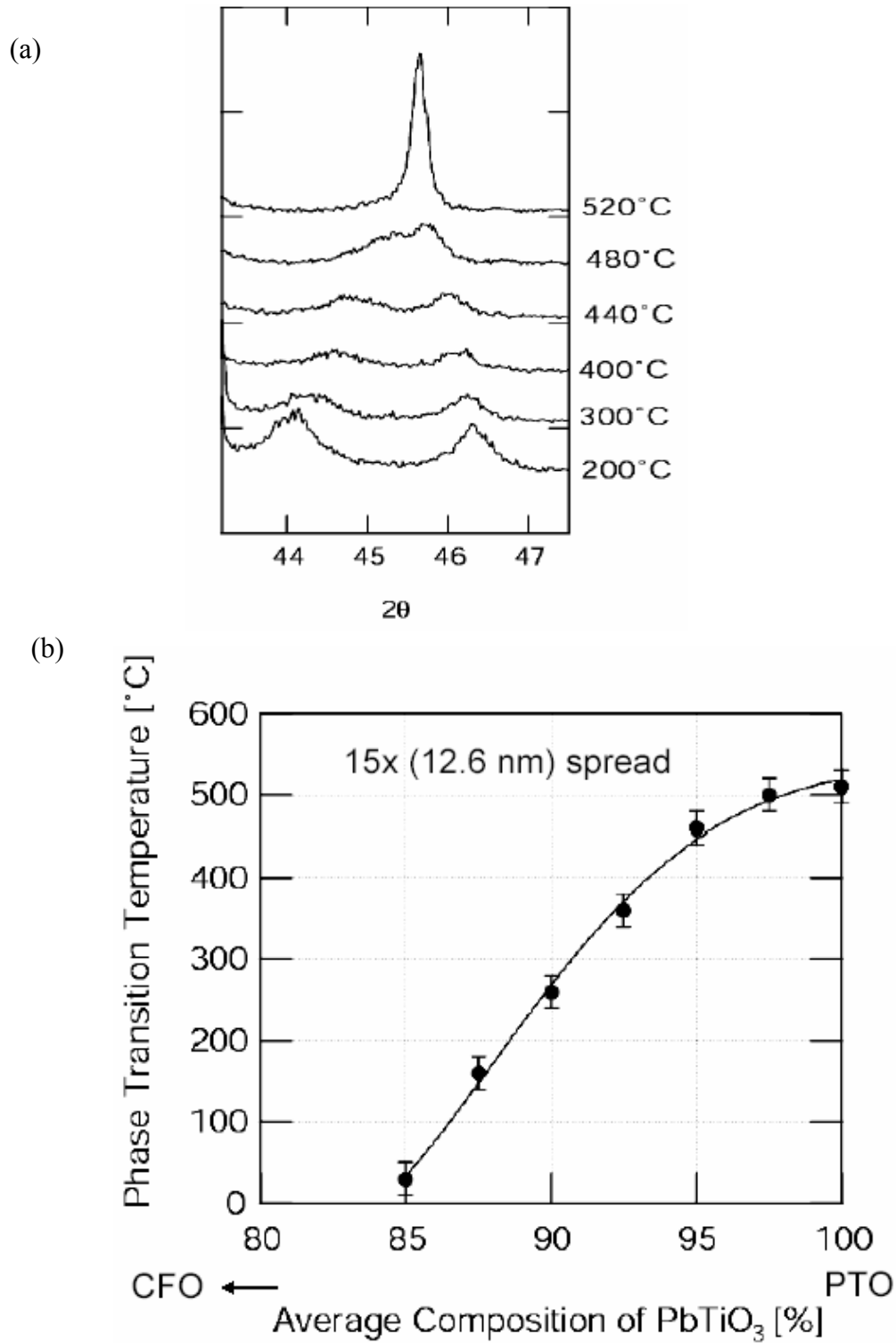


Fig. 2.15 (a) X-ray diffraction patterns for pure PTO at different temperatures. (b) The phase transition temperature T_c versus average PTO composition for 15x sample.

2.6 Characterization of magnetic properties of PTO-CFO composition spread

The room temperature scanning SQUID is used to characterize the magnetic properties across the spread samples (Fig. 2.16). The scanning SQUID microscope consists of several components: the SQUID sensor which works as a flux-to-voltage transducer, micro-positioning mechanism, a cryogenically cooled dewar, and a computer responsible for recording data and controlling the position of sample stage in order to obtain a magnetic flux distribution of a the sample. The sensor made of superconductor ($\text{YBa}_2\text{Cu}_3\text{O}_{7-x}$) is enclosed in a vacuum chamber and is thermally isolated from the atmosphere by a $25 \mu\text{m}$ sapphire window. The sample should be brought to the sample as close as possible in order to maximize the spatial resolution and the signal, and the distance between the sample and the window is typically $150 \mu\text{m}$.

We magnetize our samples in the in-plane direction although pure CFO films are known to have the out-of-plane direction as the easy axes [17]. This is because currently, we only have an algorithm that allows us to compute in-plane magnetization from magnetic field distribution. Our strategy here is to use the trend of in-plane remanent magnetization as an indication of the overall magnetic properties by mapping the field emanating from the sample [33].

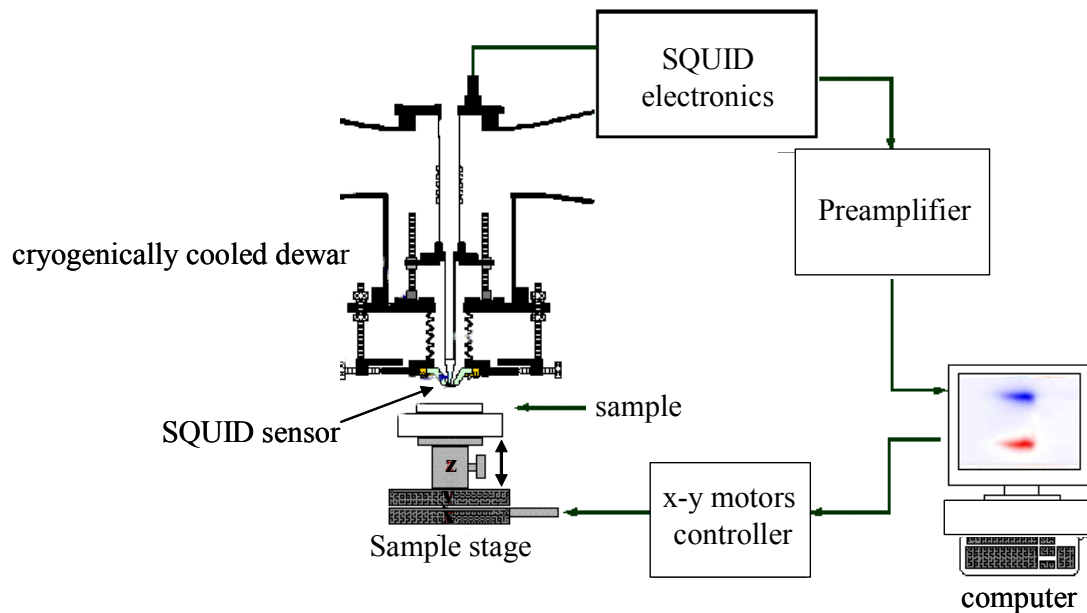
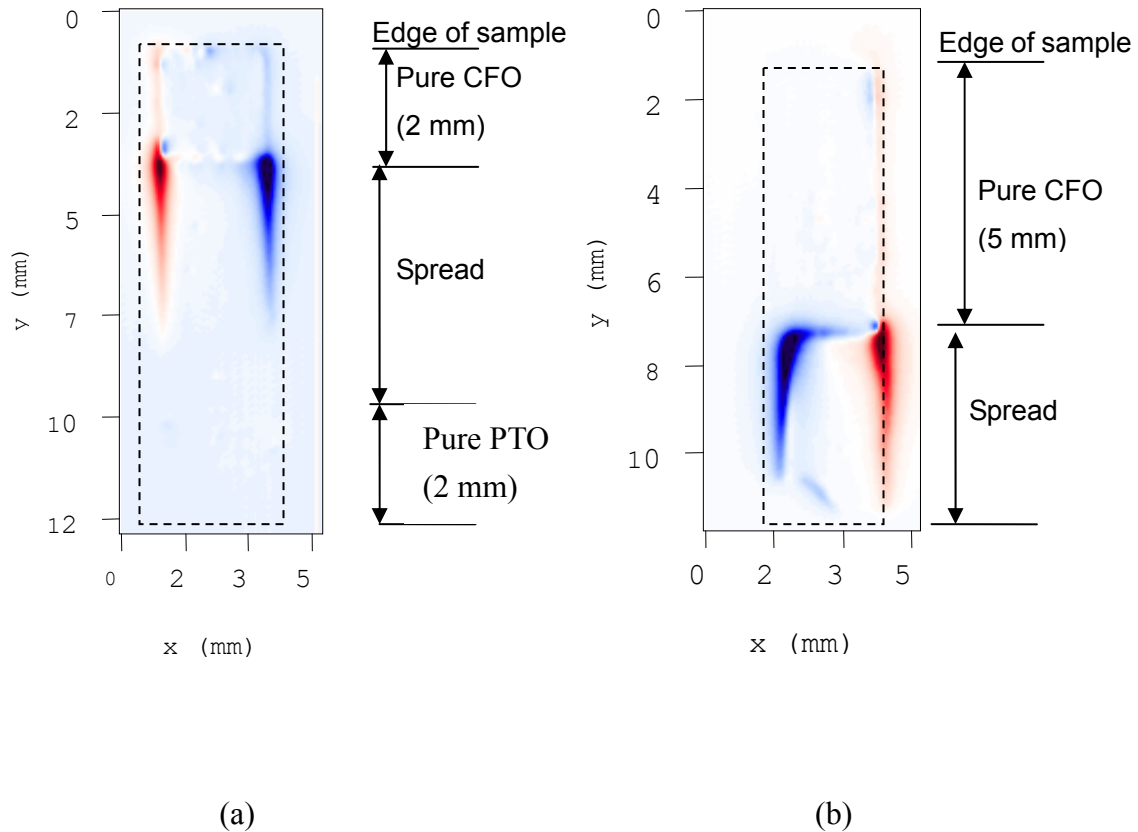


Fig. 2.16 The schematic drawing of a scanning SQUID microscope

The result shows that the composition which shows maximum remanent magnetization is not the pure CFO region. Fig. 2.17 (a) is the magnetic field image obtained by a scanning SQUID for the 15x sample magnetized in plane. The blue and red false colors correspond to the magnetic poles at the edges of the sample, and the contrast shows the intensity of magnetization. The area with light and constant color at the top of the spread is the region of the pure CFO; the area with high intense dipoles immediately below the pure CFO end is where the maximum remanent magnetization is observed. This figure clearly shows that the maximum remanet magnetization is not at the pure CFO region. In order to verify that this effect comes from materials of intended

compositions due to PLD deposition artifacts, we made a separate spread sample which is designed to have a longer region of pure CFO, and the composition spread region start at 5 mm from the edge of the sample instead of 2mm in the standard samples. The result is shown in Fig. 2.17 (b). The maximum magnetization is at the position which corresponds to the same composition where the peak is observed in standard samples. Thus this peaking behavior is a real effect which comes from the synthesized materials.



2.17 (a) Mapping of field emanating from composition spread samples obtained by a scanning SQUID microscope with a standard 15x sample. The red and blue colors represent the two poles at the opposite ends of the sample, and the contrast shows the intensity of magnetization. (b) Mapping of a special spread sample with 5mm pure CFO region at the end. The dashed lines mark where the spread is.

The position at which maximum remanent magnetization is observed occurring at $\text{PTO}_{0.85} - \text{CFO}_{0.15}$ for all samples. Fig. 2.18 shows the dependence of the measured field as a function of position (composition) for different composition spread samples. It

shows that the samples with a smaller wedge layer thickness have the higher magnetization peak value. From the literature and our experiments, CFO shows strong magnetic anisotropy. We note that the easy axis of the pure CFO thin film grown on a MgO substrate with (001) orientation is out of plane: the out-of-plane remanence is much higher than the in-plane remanence. We have made several single composition samples of pure CFO and $\text{PTO}_{0.2} - \text{CFO}_{0.8}$ which are made in the same way as compositions in the spreads. These samples are characterized using a regular SQUID to measure the M-H loop. As expected, the saturation magnetization decreases as PTO is introduced. The observed trend indicates that with increasing amount of PTO, the in-plane remanent magnetization increases and out-of-plane remanence decreases. We found that the magnetic anisotropy changes dramatically by introducing PTO into CFO. This phenomenon is clearly seen in Fig. 2.19

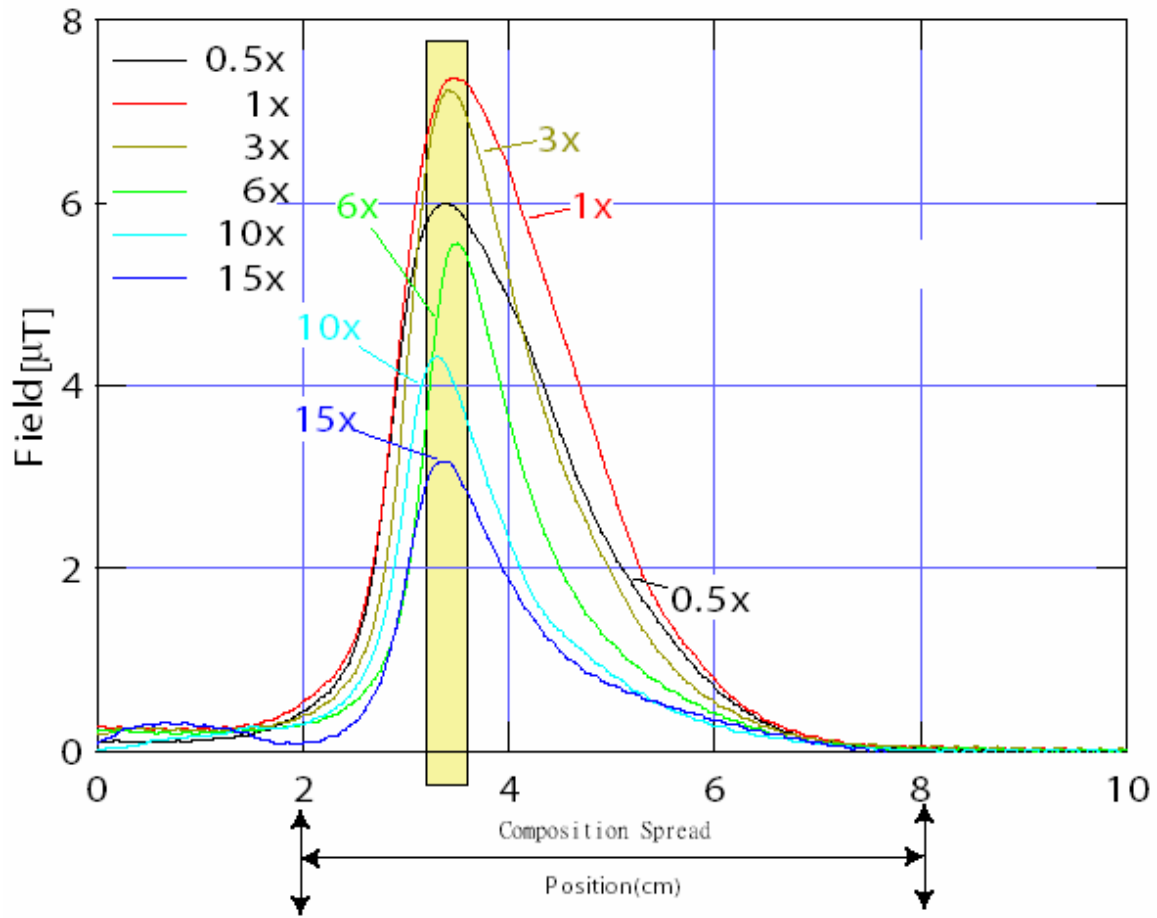


Fig. 2.18 Field measured by scanning SQUID across composition spreads. The field is due to the in-plane remanent magnetization. The bar indicates the region where the maximum field takes place.

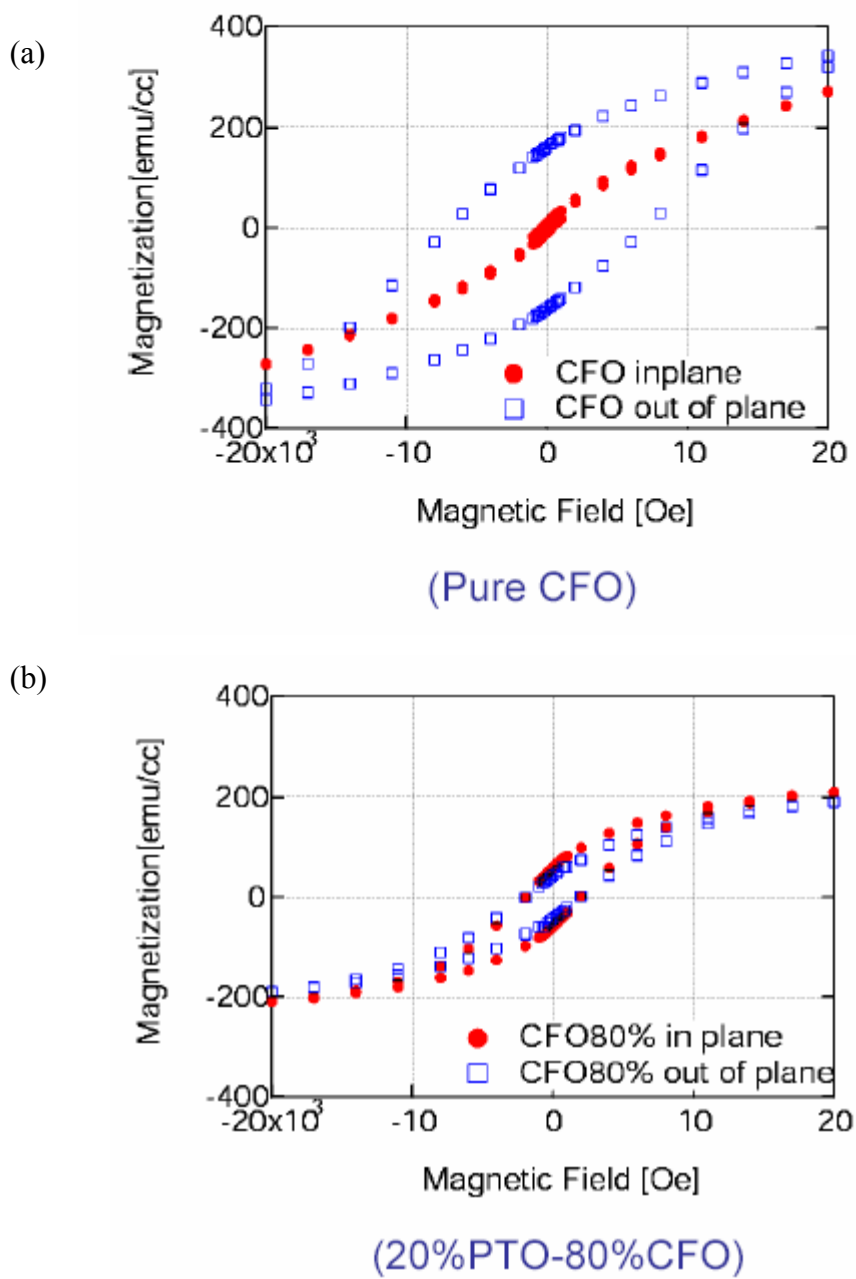


Fig. 2.19 (a) The in-plane and out-of-plane hysteresis loops for pure CFO sample. (b) The in-plane and out-of-plane hysteresis loop for $\text{PTO}_{0.2} - \text{CFO}_{0.8}$ samples. Note that the in-plane remanent magnetization of $\text{PTO}_{0.2} - \text{CFO}_{0.8}$ is larger than that of pure CFO.

The purpose of this experiment was to find a region where magnetization and ferroelectricity coexist. Fig. 2.20 plots the non-linear dielectric signal and magnetization (calculated from the measured field) as a function of composition for the 15x sample. We see that indeed we have a region that has a reasonable non-linear dielectric signal and robust magnetism coexisting in the middle of the spread.

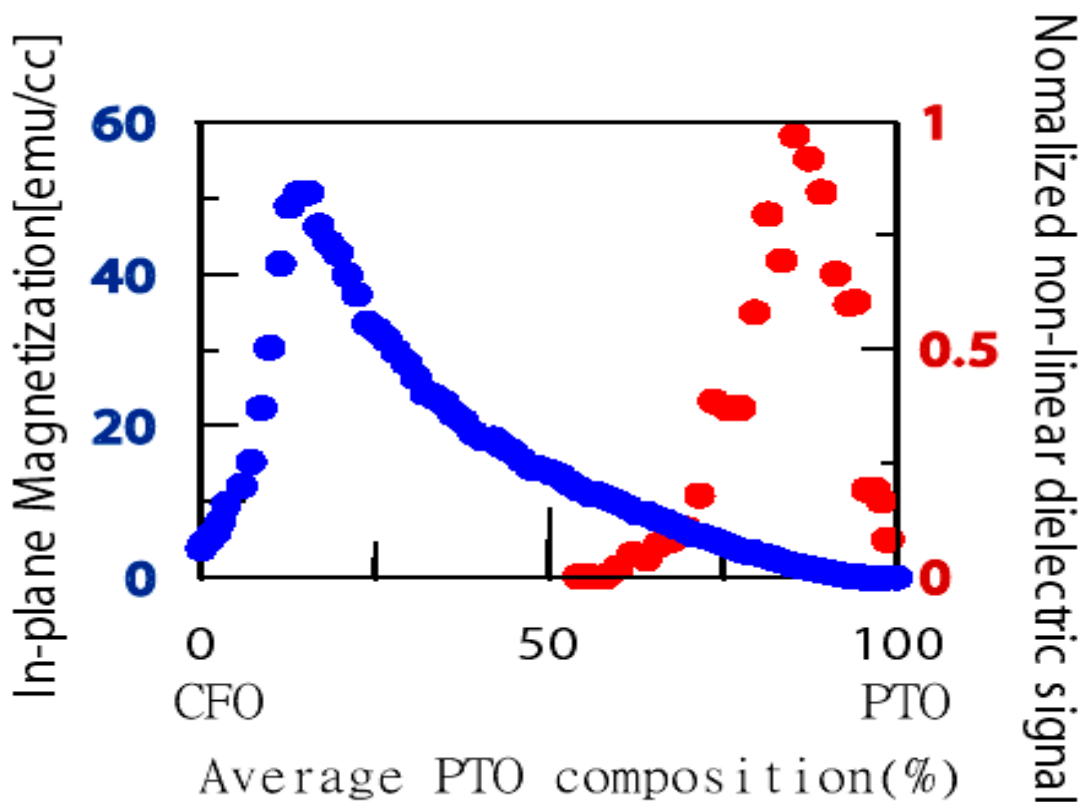
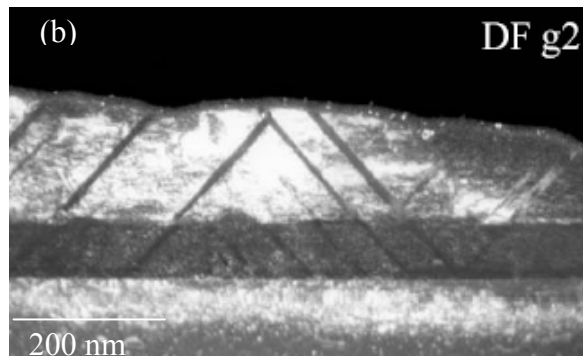
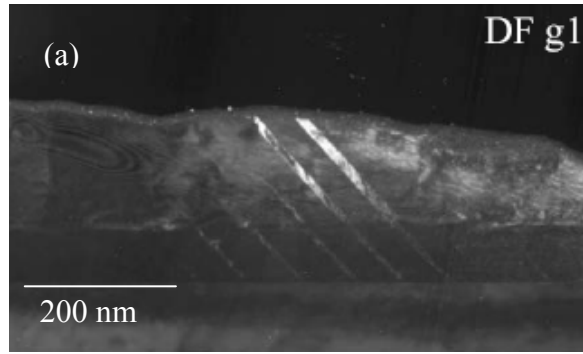


Fig. 2.20 The non-linear dielectric signal and the in-plane remanent magnetization as a function of composition across the 15x (12.6 nm) composition spread.

2.7 Transmission Electron Microscopy of PTO-CFO films

We have had TEM performed on our samples by Dr. Leo Bendersky of National Institute Standards and Technology. TEM studies provide essential information about the microstructural details of the films. The bright and dark field images give us the real space microstructure in the films, and the electron diffraction patterns give us local crystallography information about the presentation of materials at microscopic level. Such information is difficult to obtain with standard XRD.

The 15x spread sample was cut into 10 pieces which were numbered 1 to 10 from the pure PTO end, to be examined by cross sectional TEM at different compositions. From the diffraction patterns, it was confirmed that the films had grown in a heteroepitaxial way. Fig. 2.21 shows the dark-field image and the (100) diffraction pattern from the position where the composition was roughly $\text{PTO}_{0.9} - \text{CFO}_{0.1}$. Because of the tetragonal nature of PTO, there are two sets of PTO patterns which are marked as g1 and g2 in Fig. 2.21(c). They form the twin structure in the diffraction in Fig. 2.21(a), (b), and in Fig. 2.22. For this composition, we do not see any distinct CFO features. This seems to indicate that CFO and PTO have formed a solid solution at this composition. The total thickness of the film is very close to 300nm as we calculated.



(c)

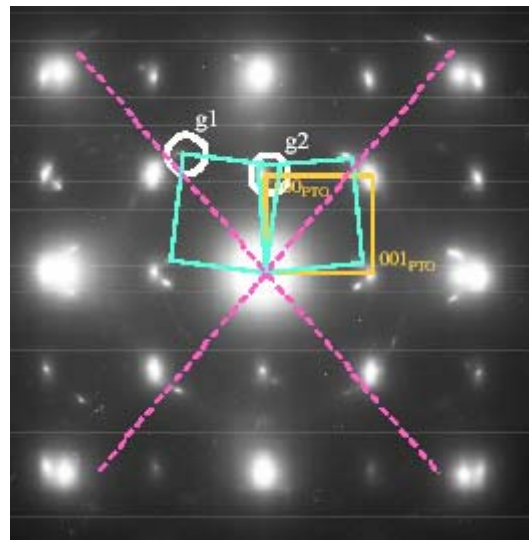


Fig. 2.21 Cross sectional TEM of the 15x composition spread taken at approximately $PTO_{0.9} - CFO_{0.1}$ (a) dark field image using g_1 vector in (c) (b) dark field image using g_2 vector (c) (100) TEM diffraction pattern.

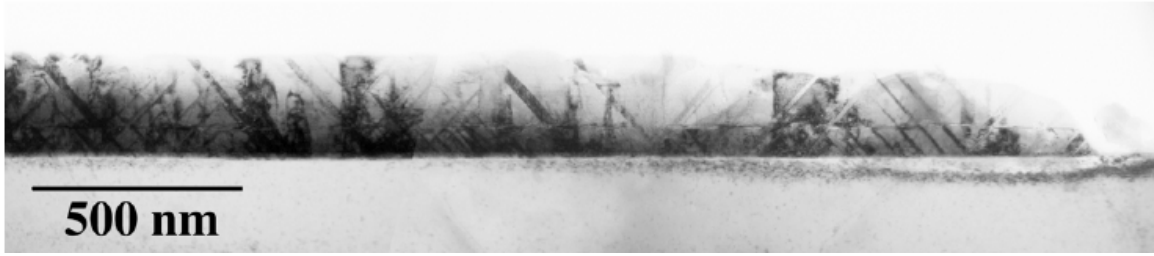
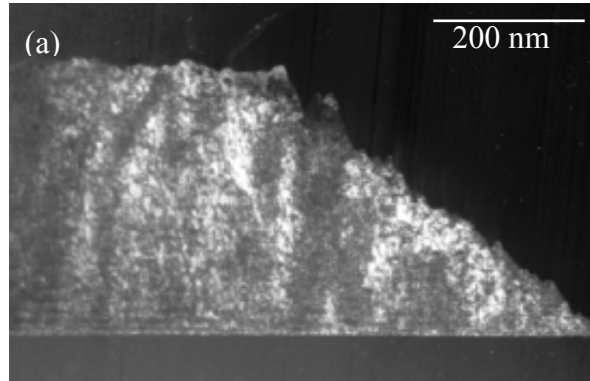


Fig. 2.22 TEM image of $\text{PTO}_{0.9} - \text{CFO}_{0.1}$ in the 15X spread sample. It shows the twin structures from the tetragonal PTO.

Fig. 2.23 is the TEM image from the 15X spread sample at the composition $\text{PTO}_{0.1} - \text{CFO}_{0.9}$ where the peak in remanent in-plane magnetization was observed. From the appearance of both PTO and CFO diffraction patterns in Fig. 2.23(c), we see that both materials coexist separated in good crystalline forms at this composition. Fig. 2.23 (a) appears to indicate presence of a layered structure near the substrate. These layered structures may be the cause of the change in anisotropy of the overall material, which in turn results in the enhanced in-plane remanent magnetization at this composition (Fig 2.19).



(b)

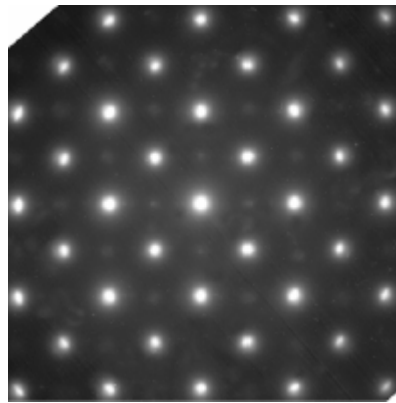


Fig. 2.23 (a) TEM image at the composition $\text{PTO}_{0.1} - \text{CFO}_{0.9}$ in 15x spread sample. The image is taken along the (110) direction (b) The (100) diffraction pattern. The bright spots belong to CFO, and the darker ones belong to PTO. Thus both materials coexist and appear to be in good crystalline forms at this composition.

We have also looked at the $\text{PTO}_{0.8} - \text{CFO}_{0.2}$ composition. In particular, we have studied this composition carefully using individually made samples with the layering thickness identical to that in the 15x composition sample. This composition is of interest because of the peak in the dielectric properties. Fig. 2.24 (a) shows the TEM image of a 15x $\text{PTO}_{0.8} - \text{CFO}_{0.2}$ single composition sample. The PTO phase appears as isolated pancake-like particles surrounded by the CFO matrix in Fig. 2.24 (a). The same image also shows the layered overall structure, which is illustrated in the cartoon: there are white thicker PTO layers “broken” by thinner dark CFO layers, and the “pancakes” resemble the way we intended to layer the structure during deposition. The diffraction patterns on this sample are shown in Fig. 2.24 (b). It shows that PTO and CFO have good crystalline structures. Due to the fact that twice the lattice constant of PTO is very close to that of CFO, we need to have both (100) and (110) diffraction patterns to distinguish and identify them. In the (100) pattern there are reflections only belonging to PTO, while only CFO gives certain reflections in the (110) pattern. The fact that CFO and PTO patterns appear in the (100) direction in (c) and the (110) direction in (d) indicates that they have good crystalline structures and that there is an epitaxial relation between them. Fig. 2.25 shows the plan view TEM image of the same sample. There are dark PTO grains surrounded by the white CFO matrix.

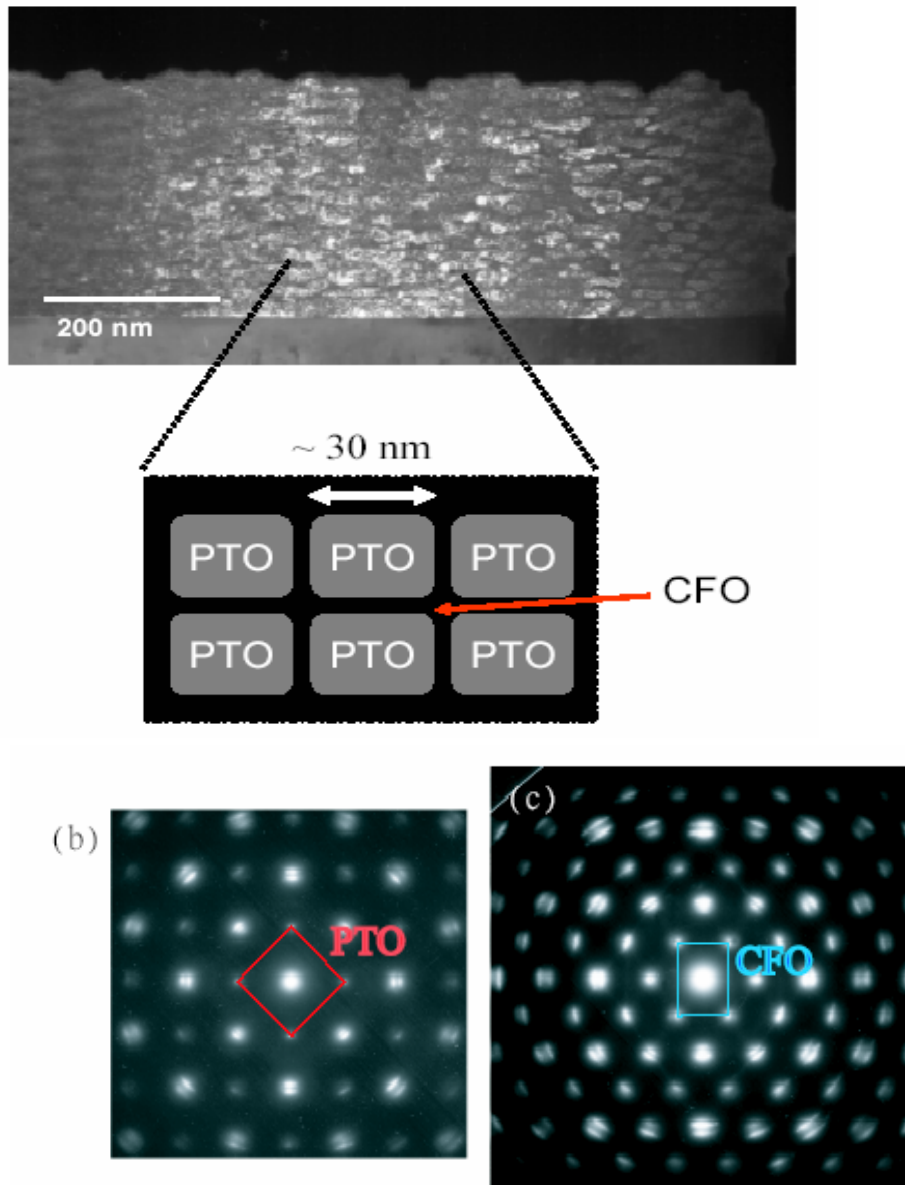
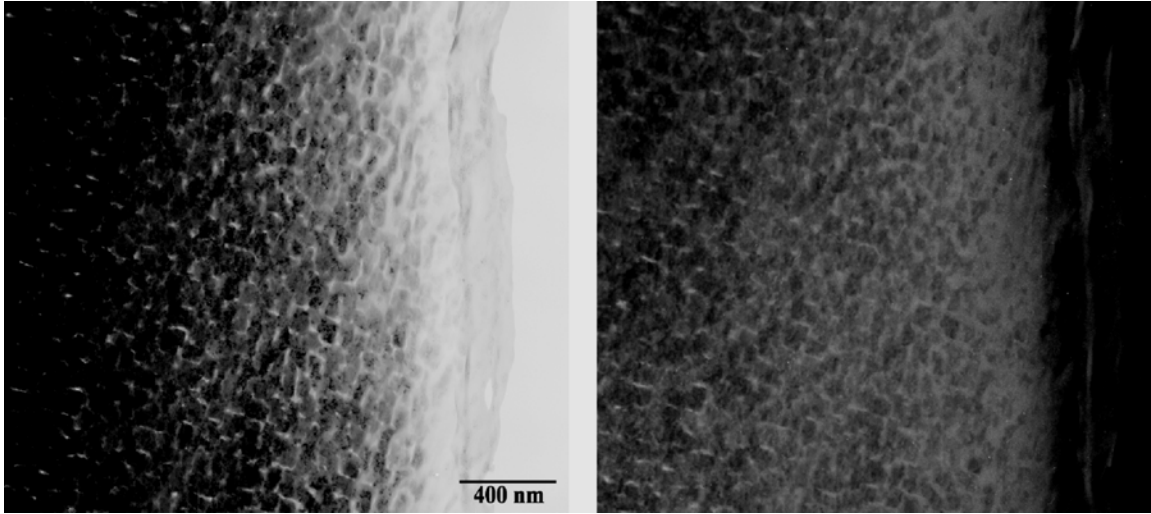


Fig. 2.24 (a) TEM image showing the cross section of a $\text{PTO}_{0.8} - \text{CFO}_{0.2}$ single composition sample. The PTO phase appears as isolated pancake-like particles surrounded by the CFO matrix. White thicker PTO layers are broken by the thinner dark CFO layers. (b) The (100) diffraction pattern showing the reflection spots only belonging to PTO. (c) The (110) diffraction pattern showing the spots only belonging to CFO.

(a)



(b)

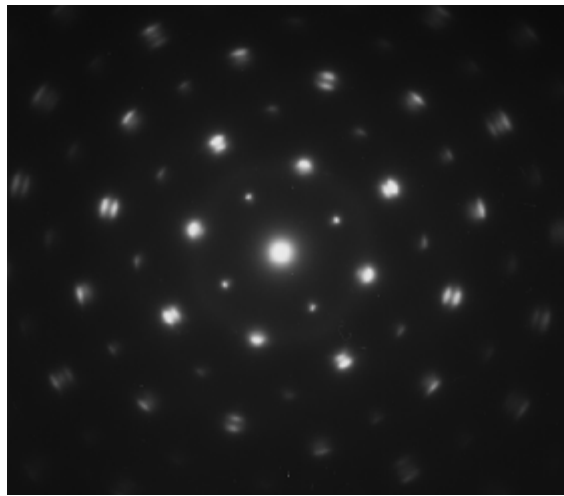
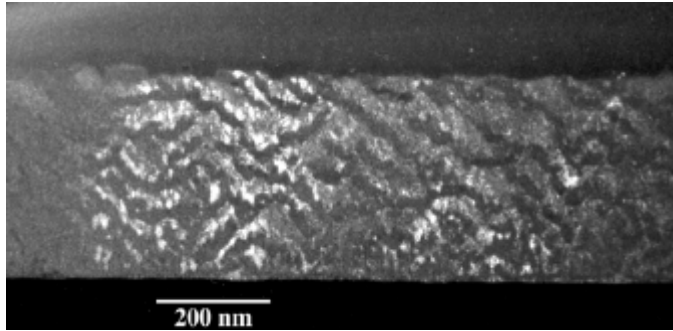


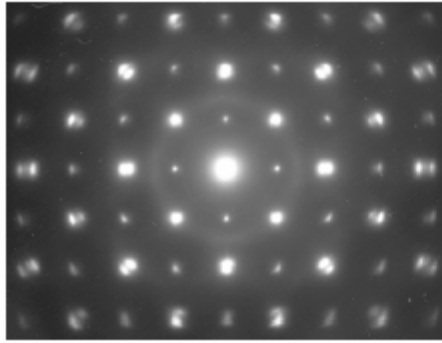
Fig. 2.25 (a) TEM image showing the plane view of a $\text{PTO}_{0.8} - \text{CFO}_{0.2}$ single composition sample. Dark PTO grains are surrounded by the white CFO matrix. (b) The (001) diffraction pattern shows the epitaxial relation between the two in this direction.

We have also looked at samples with other layering configurations. Fig. 2.26 is the TEM image from the 3x PTO-CFO spread at the composition of $\text{PTO}_{0.8} - \text{CFO}_{0.2}$. The microstructure is very different from those seen in Fig. 2.24 from the 15x sample which is at the same composition. The clear PTO island-structure doesn't exist in this case while PTO and CFO are still clearly crystalline as seen in the diffraction patterns. As we see here, samples with different layering configurations result in very different microstructure. We have thus found that 1) the microstructures of the films are drastically different from the intended superlattice structure and 2) there are regions in the "middle" of the spreads where there are clearly separated regions of CFO and PTO. These observations indicate presence of complex diffusion, phase nucleation, crystallization, and separation processes that take place during the film growth. Further TEM studies to understand the details are under way.

(a)



(b)



(c)

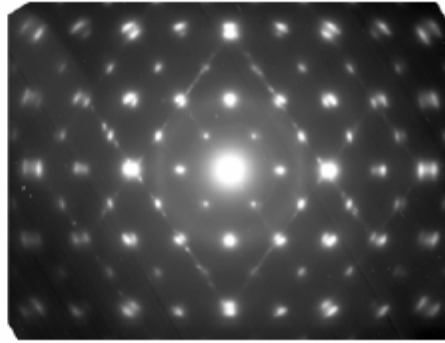


Fig. 2.26 (a) TEM image of 3x spread sample at composition 0.8PTO-0.2CFO. The structure is totally different with 15x sample at the same composition. (b) (100) diffraction pattern. (c) (110) diffraction pattern. From both diffraction patterns, PTO and CFO are seen to have good crystalline forms.

2.8 Magnetoelectric measurement

The ultimate purpose of this experiment is to discover magnetoelectric materials. We have successfully identified multiferroic compositions which exhibit strong dielectric non-linearly (which is a measure of ferroelectricity) and ferromagnetism. We believe that there is a great chance to obtain the magnetoelectric effect in this composition. There are two techniques we are using to study the occurrence of the magnetoelectric effect in our thin film samples: 1) measure the change in the dielectric properties using the microwave microscope while applying a magnetic field to the sample. An electromagnet has been mounted on the microwave microscope to perform this measurement. 2) We can measure the change in the remanent magnetization using SQUID while an electric field is applied. Both measurements are currently under way in our group.

Chapter 3 Conclusions and future work

3.1 Conclusions

The fabrication of composition spreads of artificial bi-functional thin film heterostructures consisting of alternating layers of PbTiO_3 (PTO) - CoFe_2O_4 (CFO) has been demonstrated using the combinatorial PLD system. The coexistence of ferromagnetic and ferroelectric properties has been observed in a large extended region between pure CFO and PTO. Various physical properties were measured across the composition spread. Wavelength dispersive spectroscopy (WDS) was used to verify the composition variation across the spread. An unexpected peak in the dielectric property has been observed, and it was identified as the composition where the ferroelectric phase transition takes place in PTO doped with CFO. The T_c of ferroelectricity is found to be tunable from 500°C down to room temperature by controlling the average volume ratio of CFO and PTO. We have also found that the magnetic anisotropy change dramatically by introducing PTO to CFO. Transmission electron microscopy (TEM) has been carried out to obtain microstructural information on our samples.

3.2 Future work

The biggest future challenge lies in the magnetoelectric measurements which are currently under way.

In addition to the measurement schemes described above, one can do other types of measurement if we had a bottom electrode in our samples. In particular, the bottom electrode would allow us to fabricate capacitors, which in turn would allow us to directly measure polarization as well as applying electric field in a straight forward manner (Fig 3.1). The material for the bottom electrode needs to be grown epitaxially on the substrate, and it has to allow both PTO and CFO to grow epitaxially on top. We are currently in the process of introducing a $SrRuO_3$ bottom electrode to our heterostructure.

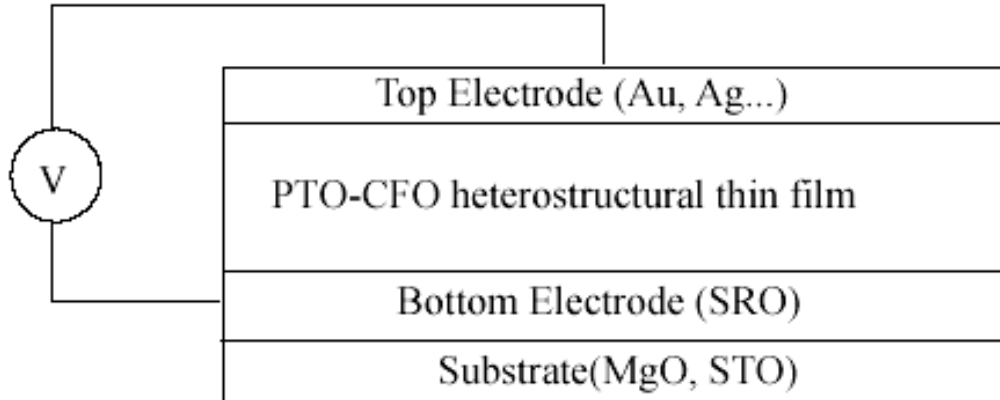


Fig. 3.1 Schematic of a parallel-plate capacitor made with our multiferroic thin film. The bottom electrode can be used to make a capacitor for the magnetoelectric measurement.

REFERENCES

1. X.-D. Xiang, and P. G. Schultz, *Physica C* **282-287**, 428 (1997)
2. X.-D. Xiang, X. Sun, G. Briceno, Y. Lou, K.-A. Wang, H. Chang, W. G. Wallace-Freedman, S.-W. Chen, and P. G. Schultz, *Science* **268**, 1738 (1995)
3. J. C. Phillips, *Physics of High-T_c Superconductors* (Academic Press, New York, 1989)
4. D. B. Chrisey, G. K. Hubler, *Pulsed Laser Deposition of Thin Films*, John Wiley & Sons, Inc., (1994)
5. K.-S. Chang, M. A. Aronova, and I. Takeuchi, to appear in *Applied Surface Science* (2003)
6. H. Chang, I. Takeuchi, and X.-D. Xiang, *Applied Physics Letters* **74**, 1165 (1999)
7. I. Takeuchi, O. O. Famodu, J. C. Read, M. A. Aronova, K.-S. Chang, C. Craciunescu, S. E. Lofland, M. Wuttig, F. C. Wellstood, L. Knauss, and A. Orozco, *Nature Materials* **2**, 180 (2003)
8. T. Fukumura, M. Ohtani, M. Kawasaki, Y. Okimoto, T. Kageyama, T. Koida, T. Hasegawa, Y. Tokura, and H. Koinuma, *Applied Physics Letters* **77**, 3426 (2000)
9. Y.-K. Yoo, F. Duewer, H. Yang, Y. Dong, J.-W. Li, and X.-D. Xiang, *Nature* **406**, 704 (2000)
10. L. D. Landau, and E. M. Lifshitz, *Electrodynamics of Continuous Media*, Gostekhizdat, Moscow (1957)
11. K.-S. Chang, Ph . D. Thesis, University of Maryland, College Park, (2004)
12. Julian Blosiu and Mary Boghosian of Caltech for NASA's Jet Propulsion Laboratory
13. N. A. Hill *Annu. Rev. Mater. Res.* 2002. 32:1–37

14. D.N Astrov, Soviet Physics JETP 12, 729(1961)
15. J. Wang, J. B. Neaton, H. Zheng, V. Nagarajan, S. B. Ogale, B. Liu, D. Viehland, V. Vaithyanathan, D. G. Schlom, U. V. Waghmare, N. A. Spaldin, K. M. Rabe, M. Wuttig, and R. Ramesh, Science **299**, 1719 (2003)
16. H. Tsujino and K. Kohn, Solid State communications, vol. 83, No. 8, pp. 639-642, 1992
17. J. Van Suchtelen, Philips Research Reports **27**, 28 (1972)
18. J. Van Den Boomgaard, A. M. J. G. Van Run, and J. Van Suchtelen, Ferroelectrics **14**, 727 (1976)
19. J. Van Den Boomgaard, A. M. J. G. Van Run, and J. Van Suchtelen, Ferroelectrics **10**, 295 (1976)
20. J. V. D. Boomgaard, and R. A. J. Born, Journal of Materials Science **13**, 1538 (1978)
21. J. V. D. Boomgaard, D. R. Terrell, R. A. J. Born, and H. F. J. I. Giller, Journal of Materials Science **9**, 1705 (1974)
22. G. Harshe, Ph. D. Thesis, Pennsylvania State University, State College (1991)
23. J. Ryu, A. V. Carazo, K. Uchino, and H.-E. Kim, Japanese Journal of Applied Physics **40**, 4948 (2001)
24. G. Srinivasan, E. T. Rasmussen, J. Gallegos, R. Srinivasan, Y. I. Bokhan, and V. M. Laletin, Physical Review B **64**, 214408-1 (2001)
25. K. Mori, and M. Wuttig, Applied Physics Letters **81**, 100 (2002). S. Dong, J.-F. Li, and D. Viehland, Applied Physics Letters **83**, 2265 (2003)
26. Y. Suzuki, G. Hu, R. B. van Dover, and R. J. Cava, Journal of Magnetism and Magnetic Materials **191**, 1 (1999)

27. W.H. Aulock, Handbook of microwave ferrite materials, 1965)
28. C. Gao and X.-D. Xiang, Review of Scientific Instruments 69, 3846 (1998)
29. T. Wei, X.-D. Xiang, W. G. Wallace-Freedman, and P. G. Schultz, Applied Physics Letters 68, 3506 (1996)
30. I. Takeuchi, T. Wei, Fred Duewer, Y. K. Yoo, X.-D. Xiang, V. Talyansky, S. P. Pai, G. J. Chen, and T. Venkatesan, Applied Physics Letters 71, 2026 (1997)
31. H. Chang, I. Takeuchi, and X.-D. Xiang, Applied Physics Letters 74, 1165 (1999)
32. H. Chang, C. Gao, I. Takeuchi, Y. Yoo, J. Wang, P. G. Schultz, X.-D. Xiang, R. P. Sharma, M. Downes, and T. Venkatesan, Applied Physics Letters 72, 2185 (1998)
33. E. F. Fleet, Ph.D. Thesis, University of Maryland, College Park (2000)